nature communications

Article

https://doi.org/10.1038/s41467-025-61455-0

Hypomyelination in autism-associated neuroligin-3 mutant mice impairs parvalbumin interneuron excitability, gamma oscillations, and sensory discrimination

Received: 3 September 2024

Accepted: 20 June 2025

Published online: 10 July 2025

Check for updates

Yongxiang He[1,7], Jiong Li[1,2,7], Wei Zheng[1,7], Junhong Liu[1,7], Zhaojun Dong[3], Lu Yang[4], Shuting Tang[1], Yanping Zou[1], Tianyu Gao[1], Yuqian Yang[1], Zhenpeng Mo[1], Shuming Wang[1], Yuehua He[1], Changyong Tang[4], Jianhong Luo[5], Jingwei Zhao[3], Guoqing Guo[2], Huiliang Li[6] & Lin Xiao[1]

Whether and how myelin plasticity, an emerging new form of brain plasticity, is involved in autism spectrum disorder (ASD) remains unknown. Here, we identify deficits in oligodendrocyte (OL) generation and myelination in the barrel cortex (BC) of the male *NL3-R451C*-KI mouse model of ASD. These mice also show impaired texture recognition, disrupted gamma neuronal oscillations, and reduced excitability and myelination level in the BC-PV interneuron. These abnormalities can be rescued by a promyelinating strategy and are recapitulated by genetic blockade of myelination in *Myrf*-cKO mice. Furthermore, OL progenitor-specific conditional *NL3* knockout mice show similar deficits in BC-PV interneuron myelination and excitability, as well as neuronal oscillation and texture recognition, closely resembling the *NL3-R451C*-KI phenotype. Collectively, these results demonstrate that *NL3* mutations commonly cause hypomyelination and reduced excitability in BC-PV interneurons, disrupting neuronal oscillation and contributing to ASD-like sensory dysfunction. Our finding reveals a mechanism underlying ASD and highlights OLs/myelin as potential therapeutic targets for ASD.

Autism spectrum disorders (ASDs) are a diverse group of neurodevelopmental disorders, the prevalence of which is increasing among young children[1]. ASDs are characterized by deficits in social interactions and communication, along with stereotyped behaviors and restricted interests. An estimated 90% of those diagnosed with ASD are also experiencing sensory anomalies[2]. The etiology of ASD and the neural mechanisms underlying these prototypical behaviors remain elusive, but studies in several ASD mouse models during the past decades have frequently found synaptic dysfunctions and disrupted excitation/inhibition (E/I) circuit balance in local neuronal connections during early brain development[3,4]. Gamma oscillations, largely influenced by parvalbumin (PV)-expressing interneurons[5], are known to play an important role in the regulation of E/I balance, and this has been suggested to be related to the social deficit in ASD patients[6,7], potentially through impaired neuronal connectivity and aberrant network formation during neural circuit development.

NL3-R451C-KI mice have been widely studied as a broad and inclusive ASD model, exhibiting multiple ASD-relevant deficits in social

A full list of affiliations appears at the end of the paper. e-mail: liuyangxiaolin@aliyun.com

novelty, hyperactivity, abnormal aggression and repetitive behaviors[8–11]. NL3 is a postsynaptic cell adhesion protein that is involved in the formation and functioning of synapses[12]. In addition to neurons, recently RNA sequencing studies have also suggested the expression of *NL3* in oligodendrocytes (OLs) and their progenitor cells (OPCs), indicating a potential role for *NL3* in OL and myelin development[13,14].

Myelin in the central nervous system (CNS) consists of multiple spiral wraps of OL plasma membrane around axons. One OL can form 50 or more individual sheaths ('internodes') around multiple axons[15,16]. This special structure enables saltatory conduction of action potentials along the axons of long-range projection neurons, facilitating rapid information transfer across large distances throughout the brain. Recently, it has been recognized that locally projecting PV interneurons can be heavily myelinated, and in a different pattern from long-range excitatory axons[17,18]. The function of myelin on the short-range axons of these interneurons is less clear, but it may facilitate and sustain rapid burst firing[18–21], which is likely to be critical for circuit development and function. In particular, a recent study suggests that myelination of PV interneurons shapes the function of cortical sensory inhibitory circuits[21]. It has been shown that new OLs and myelin continue to be generated throughout adult life and are sensitive to neuronal activity changes, in a process known as adaptive myelination or myelin plasticity, which is emerging as a new form of brain plasticity that may be actively involved in various brain functions[16,22,23]. For example, myelin plasticity has been shown to play an important role in learning and memory[24–29]. On the other hand, myelin perturbation has recently been implicated not only in classical demyelinating diseases, but also in many neurodegenerative diseases and even neurodevelopmental disorders[30–32].

Here, we show that hypomyelination of PV interneurons in the barrel cortex (BC) impairs gamma oscillations as a critical contributor to sensory dysfunction in the *NL3-R451C*-KI mice. We observed significant expression of NL3 in OL lineage cells, prompting us to investigate OL development across different brain regions and age groups in *NL3-R451C*-KI mice. This led us to uncover impaired OL maturation in the BC. We checked sensory function in *NL3-R451C*-KI mice and found a deficit in texture recognition that has not been previously reported in these mice. Interestingly, the sensory dysfunction is accompanied by disrupted gamma neural oscillations, reduced excitability of PV interneurons, and most importantly, a hypomyelination state, together with an abnormal distribution of ion channels and the initial myelin sheath in the proximal axons of PV interneurons in the BC. These defects could be largely rescued by administration of the promyelinating drug clemastine, in contrast, recapitulated by artificial blockade of myelination in *OPC-Myrf*-cKO mice. Finally, OPC-specific *NL3* knockout (OPC-*NL3*-cKO) mice phenocopied *NL3-R451C*-KI mice, showing reduced PV interneuron myelination and firing rates in the BC, along with impaired sensory behavior and abnormal neuronal oscillations. Our data suggest a critical role for *NL3* in OL/myelin development and provide detailed evidence for the involvement of OL/myelin perturbation in ASD pathophysiology.

Results

Expression of NL3 in the OL lineage cells

Although the function of NL3 has mostly been studied in neurons, such as synapse formation, existing open databases[13] suggest that *NL3* may also be abundantly expressed by the OL lineage cells. Here, using primary cultured cell samples, *NL3* mRNA levels in various types of neural cells were confirmed by RT-qPCR (Fig. 1a, b), with the results aligning well with prior RNAseq analyses, which showed that *NL3* mRNA expression is higher in OPCs compared to neurons and other glial cells[13]. Immunofluorescence staining further detected the expression of NL3 protein in OL lineage cells. In vitro observation of cultured OPCs showed that anti-NL3 immunoreactivity signals were evident in OL lineage marker-positive cells at different stages (Fig. 1c–e), exhibiting abundant co-distributed puncta of NL3 with NG2-, O4- and MBP-positive regions (Fig. 1c4–c6, d4–d6, e4–e6). Simultaneously, in vivo, NL3 expression in OPCs was characterized by diffuse localization in membrane puncta, appearing at both proximal and distal ends of PDGFRα-positive cell processes (Fig. 1f, g). Notably, NL3 reactive-puncta could also co-localize with the CC1-positive differentiated OL cell bodies without the PDGFRα signals (Fig. 1g). To clearly elucidate whether NL3 is expressed in the cell processes of individual mature OL, we administered tamoxifen to *Pdgfrα-CreER*^{T2}; *Tau*-mGFP mice[16,28] to label the newly formed OLs and the myelin sheaths they produced in the adult mice (Fig. 1h). We did see the co-localization of NL3 with GFP signals in the newly formed OL cell soma, proximal processes, and myelin sheaths (Fig. 1i). Previous work has shown that this mutation results in a 90% reduction in NL3 protein levels in total brain homogenates[33]. Consistent with this report, our immunostaining also showed a dramatic reduction (~50% decrease) in the area of co-localization between PDGFRα and NL3 in *NL3-R451C*-KI mice compared to WT mice (Fig. 1j, k), while the area of PDGFRα staining remained unchanged (Fig. 1l). Thus, NL3 is well expressed in the OL lineage cells and is down-regulated in *NL3-R451C*-KI mice, suggesting a possible role of this autism-associated gene in OL and myelin development.

Impaired OL maturation and hypomyelination in barrel cortex of *NL3-R451C*-KI mice

Next, immunostaining for CC1, ASPA, and SOX10 was performed to label differentiated mature OLs, myelinated mature OLs, and all OL lineage cells, respectively[34]. We surveyed OL development in different brain regions, including the medial prefrontal cortex (mPFC), corpus callosum, hippocampus-CA1, and barrel cortex (BC), to see if they were affected in the *NL3-R451C*-KI mice at different ages. Interestingly, we detected a brain region-specific decrease in the number of CC1- and ASPA-positive OLs in the BC of *NL3-R451C*-KI mice, particularly in the layers II/III, at postnatal day 30 (P30) and P60, but not in other brain regions examined, except for a decrease in ASPA-positive cells in the hippocampus-CA1 at P30 (Fig. 2a–d and Supplementary Fig. 1a–d). Notably, the decrease in CC1-positive differentiated OLs was observed at an even earlier stage of P14 (Fig. 2b), a time point when ASPA-positive myelinated OLs (ASPA appears later than CC1 during OL differentiation) are still very rare (Fig. 2d). The decrease in the number of mature OLs in layers II/III of the BC in P30-*NL3-R451C*-KI mice was further confirmed by in situ hybridization (ISH) using a probe targeting the myelin oligodendrocyte glycoprotein (*Mog*) gene (Supplementary Fig. 1e, f).

We next evaluated whether the reduced number of mature OLs in layer II/III BC would result in a reduction in the regional myelination level in *NL3-R451C*-KI mice. Immunostaining showed a significant decrease in the total length (Total myelin length measured within a 0.055 mm² area: P30-WT, 5.671 ± 0.1763 mm, P30-KI, 4.493 ± 0.2421 mm; P60-WT, 11.45 ± 0.5404 mm, P60-KI, 8.547 ± 1.152 mm) and fluorescence intensity of MBP+ myelin in the BC of *NL3-R451C*-KI mice at both P30 and P60 (Fig. 2e–g), indicating an insufficient myelination state. In addition, transmission electron microscopy (TEM) analysis revealed an increase in G-Ratio (Fig. 2h–k) and a decrease in the frequency of myelinated axons (Fig. 2l) in *NL3-R451C*-KI mice. Morphological examination of myelin further demonstrated a decrease in the occurrence of compacted myelin (Fig. 2m). We detected no changes in axonal diameters or density between KI and WT mice (Fig. 2n). These findings provide direct evidence of abnormal myelin development in the BC of *NL3* mutant mice.

Moreover, we measured the lengths of nodes (the non-insulated gaps between paired contactin-associated protein-positive (Caspr+) segments) and paranodes (single paired Caspr+ segments indicating uncompacted myelin lamellae located at the edge of the myelin

https://doi.org/10.1038/s41467-025-61455-0

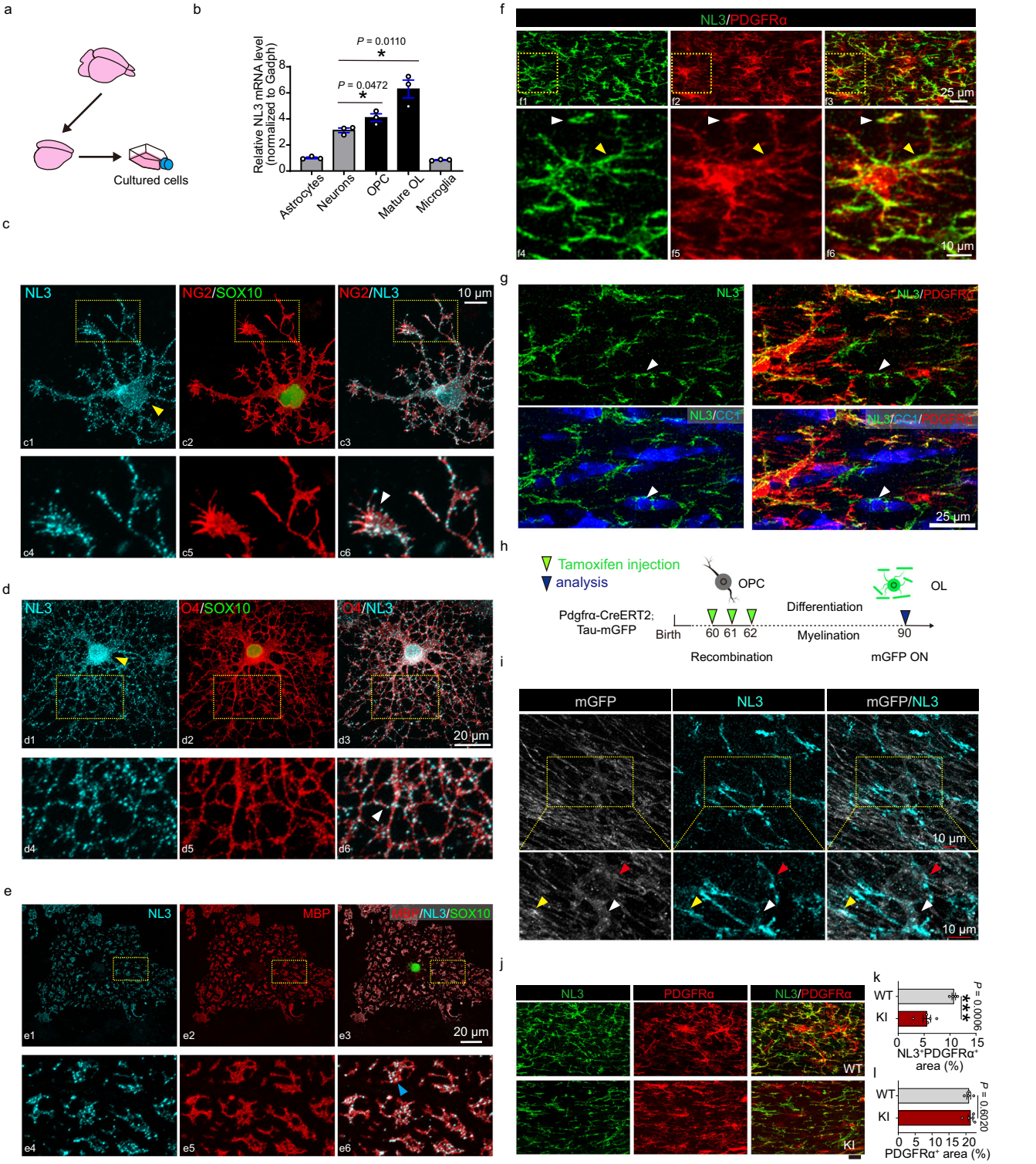

segment)[35], the myelin-related structural components that may influence axonal conductance (Fig. 2o). In layers II/III of the BC of the *NL3-R451C*-KI mice, there was a decrease in the proportion of paranode with lengths ranging from 1.2 μm to 1.5 μm, and a minimal shift toward the shorter direction in the length distributions for all paired paranodes, corresponding to an ~2.7% decrease in the median value (Fig. 2p). There was also a decrease in the proportion of nodes with lengths ranging from 1.2 μm to 1.5 μm (Fig. 2q), along with a reduction in the average number of nodes (Fig. 2r).

These results reveal impaired OL maturation and reduced myelin development in layer II/III of the BC in *NL3-R451C*-KI mice.

Decreased OL lineage cell proliferation and differentiation in the barrel cortex of *NL3-R451C*-KI mice

To elucidate the underlying mechanism of the impaired OL maturation and consequent hypomyelination in the BC of *NL3-R451C*-KI mice, we investigated whether there was a deficiency in the proliferation or differentiation of OL lineage cells.

BrdU was administered to mice in vivo at different ages and using different administration paradigms to trace OL lineage cell proliferation (Fig. 3a–c and Supplementary Fig. 2). This revealed significant reductions in the densities of both $SOX10^+/BrdU^+$ proliferating OL lineage cells (Fig. 3c) and $SOX10^+$ total OL lineage cells (Fig. 3d) at both P30 and P60

Fig. 1 | NL3 is expressed in the OL lineage. a Primary cultures of different cell types derived from the cortex of P0 mice by the mixed glial method or neurons from E16 mice. **b** qRT-PCR analysis of *NL3* expression in different cell types in primary cultures (6 wells/samples from 3 mice cultures). **c**–**e** Immunostaining for NL3 across different stages of oligodendrocyte development in vitro revealed its expression in OPC (marked by NG2 (red)), immature OL (marked by O4 (red)), and mature OL (marked by MBP (red)). NL3 (cyan) staining was observed in the cell bodies (yellow arrows) and processes (white arrows) of NG2+ and O4+ cells, as well as on MBP+ myelin sheaths (blue arrows). **f** Immunostaining for NL3 (green) and PDGFRα (red) displaying the expression of NL3 in OPCs of white matter. NL3 staining is distributed along the proximal processes of OPCs (yellow arrow) as well as the distal processes (white arrow). **g** Immunostaining for NL3 (green) and CC1 (blue) displaying the expression of NL3 in mature OL in white matter. NL3 staining is mainly localized around the cytoplasm (white arrow). **h** Schematic illustration showing the time course for tamoxifen induction and mGFP expression in the PDGFRα-CreER^{T2}; Tau-mGFP mice. **i** Immunostaining for NL3 (cyan) and mGFP (white) displaying the expression of NL3 in mature OL of white matter. Magnified images (lower) showing expression of NL3 in the cell body (red arrow), proximal processes (white arrow), and myelin sheaths (yellow arrow). **j**–**l** Immunostaining for NL3 (green) and PDGFRα (red) displaying the expression of NL3 in OPC of white matter in WT and KI mice (**j**). Quantification of NL3 + PDGFRα+ area (**k**) and PDGFRα+ area (**l**) in white matter at the age of P60 (WT/KI = 4/5 mice). The co-localization area of NL3 and PDGFRα in KI mice decreased, thereby decreasing NL3 protein expression in OPC. All data are shown as mean ± SEM; *P*-values were obtained by 2-tailed unpaired Student's *t*-test. Source data are provided as a Source Data file.

in the BC of *NL3-R451C*-KI mice, while not in other brain regions except in the corpus callosum at P30 (Supplementary Fig. 2c). In vitro culture experiments also demonstrated a decrease in the proliferative capacity of OL lineage cells derived from *NL3-R451C*-KI mice (Supplementary Fig. 3a–e). Consistently, ISH revealed a decrease in the density of *Pdgfrα*-positive OPCs in the BC of *NL3-R451C*-KI mice at P60 (Fig. 3f, g and Supplementary Fig. 2d, e). Thus, impaired OL lineage cell proliferation might contribute to the decrease in the number of mature OLs and the consequent hypomyelination in the BC of *NL3-R451C*-KI mice.

To ascertain whether the differentiation ability of OPCs is also affected in the *NL3-R451C*-KI mice, we conducted a BrdU-based cell differentiation tracing assay (Fig. 3h). The results showed a decrease in both the total number and relative proportion of newly generated mature OLs, identified as ASPA$^+$/BrdU$^+$/SOX10$^+$ within the population of BrdU$^+$/SOX10$^+$ cells in *NL3-R451C*-KI mice at P30 (Fig. 3h–k), demonstrating that fewer OPCs that had previously proliferated and incorporated BrdU had matured to ASPA$^+$-stage OLs over the following 2 weeks, suggesting an impaired differentiation capacity for their OPCs. This impairment was further confirmed in an in vitro culture system of OPCs derived from either *NL3-R451C*-KI or control mice (Supplementary Fig. 3f). There was an increase in the proportion of NG2$^+$ OPCs and a decrease in both the number and proportion of MBP-positive cells (Supplementary Fig. 3j–l) and, most intriguingly, a significant decrease in the proportion of OLs with highly developed MBP+ sheet structures which resembles the stage 4 OLs that have been previously described in vitro[36–38], while more cells remained at a low branching complexity in the cultures from *NL3-R451C*-KI mice (Supplementary Fig. 3m, n). Notably, there was still a reduction in CC1$^+$/EdU$^+$/SOX10$^+$ newly generated mature OLs (Supplementary Fig. 4a–e), as well as a diminished total number of CC1$^+$SOX10$^+$ cells in the BC of *NL3-R451C*-KI mice at P160 (Supplementary Fig. 4f), indicating a long-lasting impairment of OL differentiation and insufficiency of mature OLs. Given the observed decline in BrdU$^+$ or EdU$^+$ newly generated OLs, we performed ISH for *Enpp6*, a marker of newly forming OLs[29], to confirm the deficiency in OL production in *NL3-R451C*-KI mice. We did detect a decrease in the number of *Enpp6*-positive cells in the BC of *NL3-R451C*-KI mice at both P14 and P30 (Fig. 3l–n).

Thus, the observed impairment in OL/myelin development in the BC of *NL3-R451C*-KI mice may result from a combination of deficits in OL lineage proliferation and differentiation, given that these two processes are tightly linked and interdependent[39].

Deficient tactile discrimination in *NL3-R451C*-KI mice coincides with abnormal c-Fos hyperactivation in the layer II/III of the barrel cortex

Abnormal myelin development in the BC of *NL3-R451C*-KI mice might indicate potential deficits in whisker-dependent tactile behaviors. As a previous study suggested that *NL3-R451C*-KI mice have normal recognition memory for novel objects of different shapes[10], we here introduced a modified behavioral task of novel object recognition that relies solely on tactile sensation, where the new objects are identical to the familiar ones but have only subtle variations in surface texture (fine and coarse sandpaper)[21]. In this model, the potential bias towards specific surface textures in WT and *NL3-R451C*-KI mice was ruled out, as each object with distinct textures was equally perceptible and preferred by the mice during the first contact (Fig. 4a, b). During the learning phase, both WT and *NL3-R451C*-KI mice explored identical objects for comparable durations (Fig. 4e, f). In the subsequent test involving the presence of a novel object, WT mice discriminate between different textures by showing increased exploration of the novel object compared to the familiar one (Fig. 4e, f). Intact whiskers are essential for this discrimination as mice subjected to bilateral whisker trimming showed no preference for the novel texture (Supplementary Fig. 5). However, in the testing phase, *NL3-R451C*-KI mice showed no preference for the novel object as WT mice did (Fig. 4e, f), suggesting that they were unable to discriminate between objects that were similar but differed only in surface texture, due to impaired tactile sensory function.

Within the column corresponding to the intact whisker, approximately 17% of layer II/III pyramidal neurons encode whisker movements[40]. Subsequently, we accessed the activation of these neurons in layer II/III of BC following the tactile discrimination task by detecting the expression of the immediate-early gene product c-Fos in CUX1-positive cells, which marks the cortical pyramidal neurons in layers II–IV[41]. Interestingly, *NL3-R451C*-KI mice showed increases in both the total number of c-Fos$^+$/CUX1$^+$ cells and in the proportion of c-Fos$^+$ cells among all CUX1$^+$ cells during texture exploration (Fig. 4g–j; Supplementary Fig. 8a–d), whereas they remained unchanged in the resting state without texture exploration (Supplementary Fig. 8e–h), suggesting a task-related hyperactivity of pyramidal neurons in concomitant with the impaired sensory dysfunction in tactile discrimination in the KI mice.

Dysfunction of tactile discrimination-related neuronal oscillations in the layer II/III barrel cortex of *NL3-R451C*-KI mice

To further investigate the possible abnormalities in task-related neuronal activation within the barrel cortex region of *NL3-R451C*-KI mice, we introduced in vivo electrophysiological recording of local field potential (LFP) in layer II/III of the BC during free texture exploration (Fig. 5a). Interestingly, during exploration, *NL3-R451C*-KI mice showed a significant reduction in the gamma band activity (55–90 Hz) compared to WT mice (Fig. 5b, g), while the power of other frequency bands remained unchanged (Fig. 5c–f). Interestingly, previous research has shown that cuprizone-induced demyelination leads to a reduction in cortical gamma oscillation power in mice[19].

A role for cross-frequency coupling (CFC) in neuronal signal processing has been proposed[42]. For instance, in theta-to-gamma phase-amplitude coupling (PAC), the amplitude of a fast signal is influenced by the phase of a slow signal, quantified by the mean vector length (MVL) (Fig. 5i)[43]. To determine whether this coupling is disrupted in *NL3-R451C*-KI mice, we initially employed conventional PAC algorithms to assess the strength of coupling between the phase of the theta band at each epoch and the corresponding amplitude (envelope) of the gamma band over time. Subsequently, the average modulation

https://doi.org/10.1038/s41467-025-61455-0

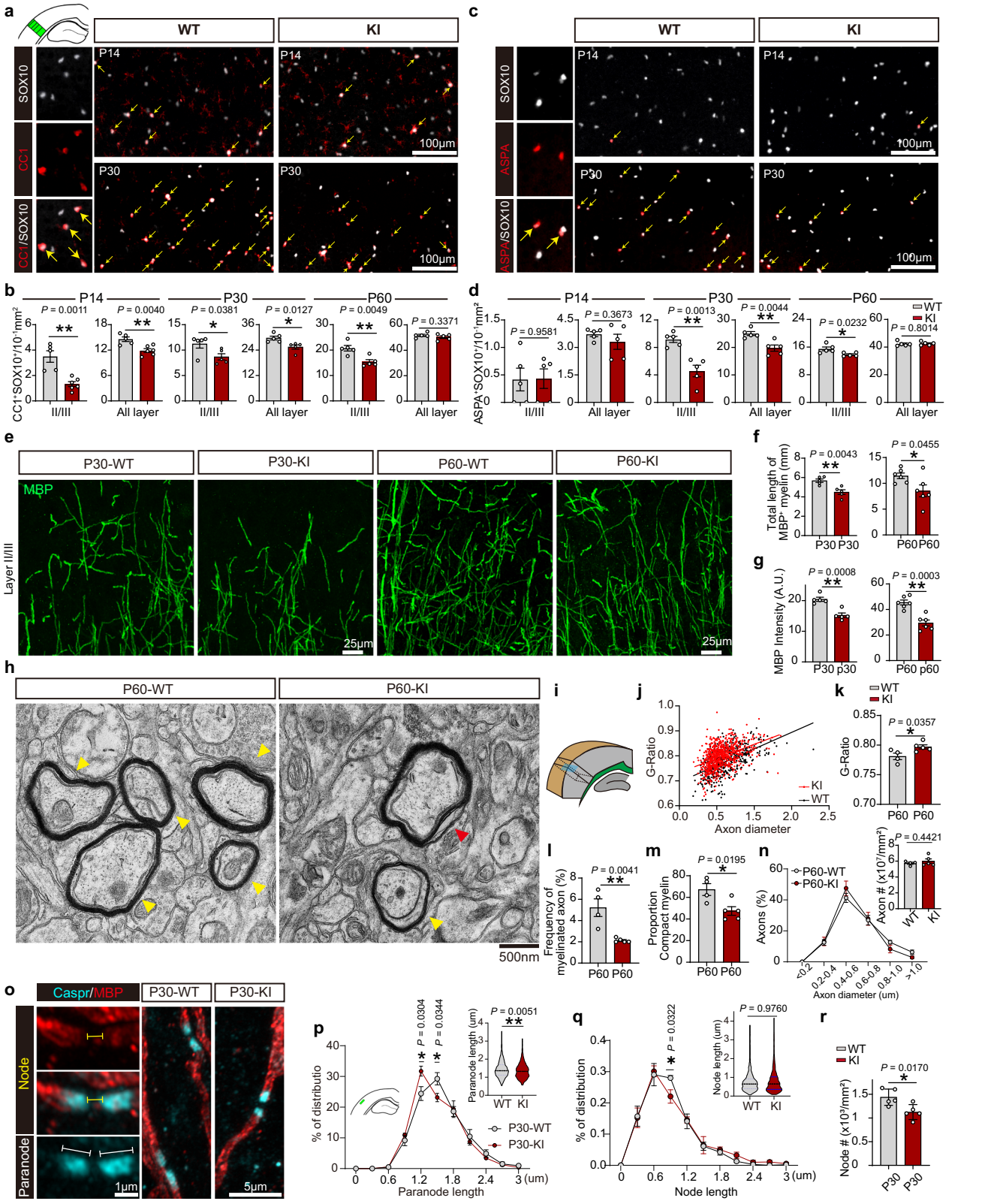

strength of theta band phase on high-gamma band amplitude was compared between WT and *NL3-R451C*-KI mice. Conventional comodulogram analysis of PAC in the layer II/III BC demonstrated that during exploration, LFPs from WT mice exhibited pronounced modulation of high-gamma (55–85 Hz) amplitudes by theta phase (Fig. 5j, k). However, in *NL3-R451C*-KI mice, the coupling between high-gamma amplitude and theta phase was significantly diminished, suggesting an impairment in the integration of temporal information within the local neural circuits of these mice (Fig. 5j, k).

We also employed oscillation-triggered coupling (OTC) analysis to further investigate PAC[44,45]. OTC utilizes a data-driven approach, treating high-frequency neuronal oscillations as discrete burst events (Fig. 5l) and overlaying the corresponding raw LFPs to derive the modulatory signal (Fig. 5m). During exploration, we observed a

Fig. 2 | Hypomyelination and reduced number of mature oligodendrocytes in the barrel cortex of KI mice. a–d Immunostaining for CC1 (**a**) and ASPA (**c**) displaying mature OLs in BC layer II/III; yellow arrows indicating colocalized $CC1^+SOX10^+$ (red/white) or $ASPA^+SOX10^+$(red/white). Quantification of $CC1^+$ OLs (**b**) and $ASPA^+$ OLs (**d**) in different layers of BC at the age of P14, P30 and P60. In (**b**), p14: WT/KI = 5/6 mice; p30 and p60: WT/KI = 5/5 mice. In (**d**), $n = 5$ mice/group. **e–g** Representative IHC images (**e**) displaying MBP (green) expression in BC layer II/III at P30 and P60. Quantification of MBP length (**f**) and density (**g**) in BC layer II/III. In (**f**) and (**g**), p30: $n = 5$ mice/group; p60: $n = 6$ mice/group. **h** TEM micrographs of myelin in layer II/III of BC in WT and KI mice (Compacted myelin, yellow arrow; Uncompacted myelin, Red arrow). **i** The image depicts the cross-sectional orientation and location (the blue planar that parallels the green subcortical white matter region) for tissue sample preparation for transmission electron microscopy, specifically focusing on the BC layer II/III. **j–n** Quantification of individual G-Ratio distribution (**j**, linear regression), G-Ratio average (**k**), proportion of myelinated axons (**l**), proportion of compacted myelin (**m**), axonal diameters and density (**n**) in the layer II/III BC (**k–n**: WT/KI = 4/5 mice). **o–r** Representative confocal images of single nodes of Ranvier flanked by Caspr (cyan) expressing paranodes of axons labeled MBP (red) in WT and KI mice BC layer II/III at P30. Quantitative analysis of paranode length (**p**), node length (**q**) and node number (**r**) in BC layer II/III at P30 ($n = 5$ mice/group). All data are shown as mean ± SEM. Statistical analyses of results in (**b**), (**d**), (**f**), (**g**), (**k**), (**l**), (**m**), (**n**), and (**r**) were evaluated with 2-tailed unpaired Student's *t*-test; Statistical analyses of results in (**p**) and (**q**) were evaluated with two-way ANOVA and Bonferroni's multiple-comparisons test. Violin plots of paranode and node length were evaluated with MWU 2-tailed test. Source data are provided as a Source Data file.

weakened modulation strength between high gamma and theta in *NL3-R451C*-KI mice (Fig. 5n), while there was no significant alteration in the phase of the modulatory signal (Fig. 5o), suggesting that these mice may experience reduced coordination of local cortical network activity in the BC during exploratory behavior.

To further investigate the relationship between LFP signals and behavior, we compared high gamma power and theta-gamma PAC strength during the exploration of familiar and novel textures. Within each group, no significant differences were observed in high gamma power or PAC strength between familiar and novel texture exploration (Supplementary Fig. 9a–c). However, *NL3-R451C*-KI mice showed significantly lower high gamma power and PAC strength compared to WT mice when exploring both familiar and novel textures (Supplementary Fig. 9a–c). In addition, correlation analysis revealed a significant positive correlation between the exploration index and the theta-gamma PAC strength during the testing phase (Supplementary Fig. 9d), suggesting that stronger PAC is associated with more exploratory behavior.

These data strongly suggest that impaired high gamma oscillations and disrupted local phase-amplitude coupling function were associated with sensory dysfunction in *NL3-R451C*-KI mice.

Hypomyelination and reduced excitability of layer II/III PV interneurons in the barrel cortex of *NL3-R451C*-KI mice

Since PV interneurons are critical for the generation of gamma rhythms and cross-frequency coupling between theta and gamma rhythms, which are crucial for sensory processing[10,46,47], we wonder whether the abnormal neuronal oscillations in the BC of *NL3-R451C*-KI mice are associated with PV interneuron dysfunction. We investigated their excitability by patch-clamp recordings of ex vivo brain slices from G42-crossed (with PV interneurons labeled by GFP) *NL3-R451C*-KI and control mice (Fig. 6a). We found a significant decrease in the intrinsic excitability of BC-PV interneurons (layer II/III) in KI mice in response to step-current injection (Fig. 6b, c). They also exhibited a more hyperpolarized resting membrane potential (by ~4 mV) without a change in the apparent input resistance, and a significantly higher rheobase (by ~59 pA), as well as a ~ 3 mV more hyperpolarized AP voltage threshold (Supplementary Table 1), all indicative of their reduced excitability. To further confirm this issue in vivo, we assessed PV interneuron activation by quantifying PV^+c-Fos^+ double-positive cells. The results showed a significant reduction in both the number and proportion of PV^+c-Fos^+ double-positive cells in *NL3-R451C*-KI mice after tactile behavioral tasks (Supplementary Fig. 8i–l), suggesting a reduced PV interneuron activity during the sensory task. As PV interneurons exert robust inhibition on postsynaptic pyramidal neurons, we next examined the miniature postsynaptic currents (mIPSCs) from the pyramidal neurons in layer II/III of the BC and found a significant decrease in both their frequency and amplitude in KI mice (Supplementary Fig. 10i–k), which is in good agreement with the observed increase in $CUX1^+$c-Fos^+ activated cells in this region (Fig. 4g–j, Supplementary Fig. 8a–d). Thus, the excitability of BC-PV interneurons (layer II/III) was reduced in *NL3-R451C*-KI mice, accompanied by reduced inhibitory synaptic transmission input to pyramidal cells.

We next asked why PV interneuron excitability is reduced in *NL3-R451C*-KI mice. It has been shown that PV interneurons are the most abundantly myelinated neurons in the BC (layer II/III)[18,48,49], and both insufficient or abnormal myelination of PV interneurons could result in their reduced excitability[19,21]. Since we have observed an overall reduction in OL cell number and myelination level in the BC (layer II/III) of KI mice (Fig. 2a–g), we then carefully examined the myelination level of PV interneurons in this region by triple immunostaining for PV, MBP and Caspr. MBP labeled the myelin sheaths, and MBP positivity flanked by Caspr positivity at both ends was considered as a full myelin internode; otherwise, it was considered as a myelin fragment (Fig. 6d). Both myelin fragments and internodes specifically colocalized with PV staining were regarded as myelin of PV interneurons (PV+ myelin). The results showed a significant decrease in the number of PV internodes (Fig. 6e), and in the total length of PV+ myelin (measured within a 0.055 mm^2 area: P30-WT, 2.305 ± 0.2936 mm; P30-KI, 1.424 ± 0.2301 mm) in the layer II/III BC of *NL3-R451C*-KI mice at P30 (Fig. 6f). In agreement with previous studies[21], PV internodes with lengths between 10 μm and 40 μm were the most abundant, accounting for ~83% of the total in the layer II/III of the BC at P30 in WT mice (Fig. 6g), whereas there was a decrease in the proportion of PV internodes with lengths in the range of 10–20 μm and 30–40 μm, but an increase in the range of 40–50 μm (Fig. 6g), ultimately leading to an increase in the average length of PV internodes in KI mice (Fig. 6h). Notably, the reduced total length of PV+ myelin (P60-WT, 3.039 ± 0.2374 mm; P60-KI, 1.532 ± 0.3505 mm) persisted at least until P60 (Fig. 6j, k). To assess the degree of myelination of PV interneurons in this region in a more direct and precise manner, we further performed immunogold EM experiments to analyze PV+ myelin in cross-sections of BC layer II/III. Our results showed that in KI mice, the density of PV+ immunogold-labeled myelinated axons was significantly reduced compared to WT mice (Fig. 6m, n, p), while the density of PV+ immunogold-labeled axons remained unchanged (Fig. 6o), clearly demonstrating the hypomyelination state of PV interneurons. Furthermore, our triple staining for PV, MBP, and Caspr also revealed a significant increase in the length of the nodes of Ranvier in the BC of KI mice (Fig. 6r), whereas the paranodal length remained unchanged (Fig. 6s), suggesting an altered myelination pattern of PV+ axons in the BC.

Previous studies have reported a reduced density of PV interneurons in hypomyelinated mice in the auditory cortex[20]. To rule out the potential effect of abnormal development of the PV interneurons themselves, we assessed both the area of PV protein immunofluorescence reactivity (PV+ area) and the number of PV+ cells in the BC (layer II/III). Our results showed no differences in either the PV+ area or the number of PV+ cells between WT and KI mice at P14, P30 and P60 (Fig. 6i, l, Supplementary Fig. 6a–d). Furthermore, there were no differences in either the total length of PV interneuron axons identified by co-immunolabelling for NF200 (neurofilament 200) and

https://doi.org/10.1038/s41467-025-61455-0

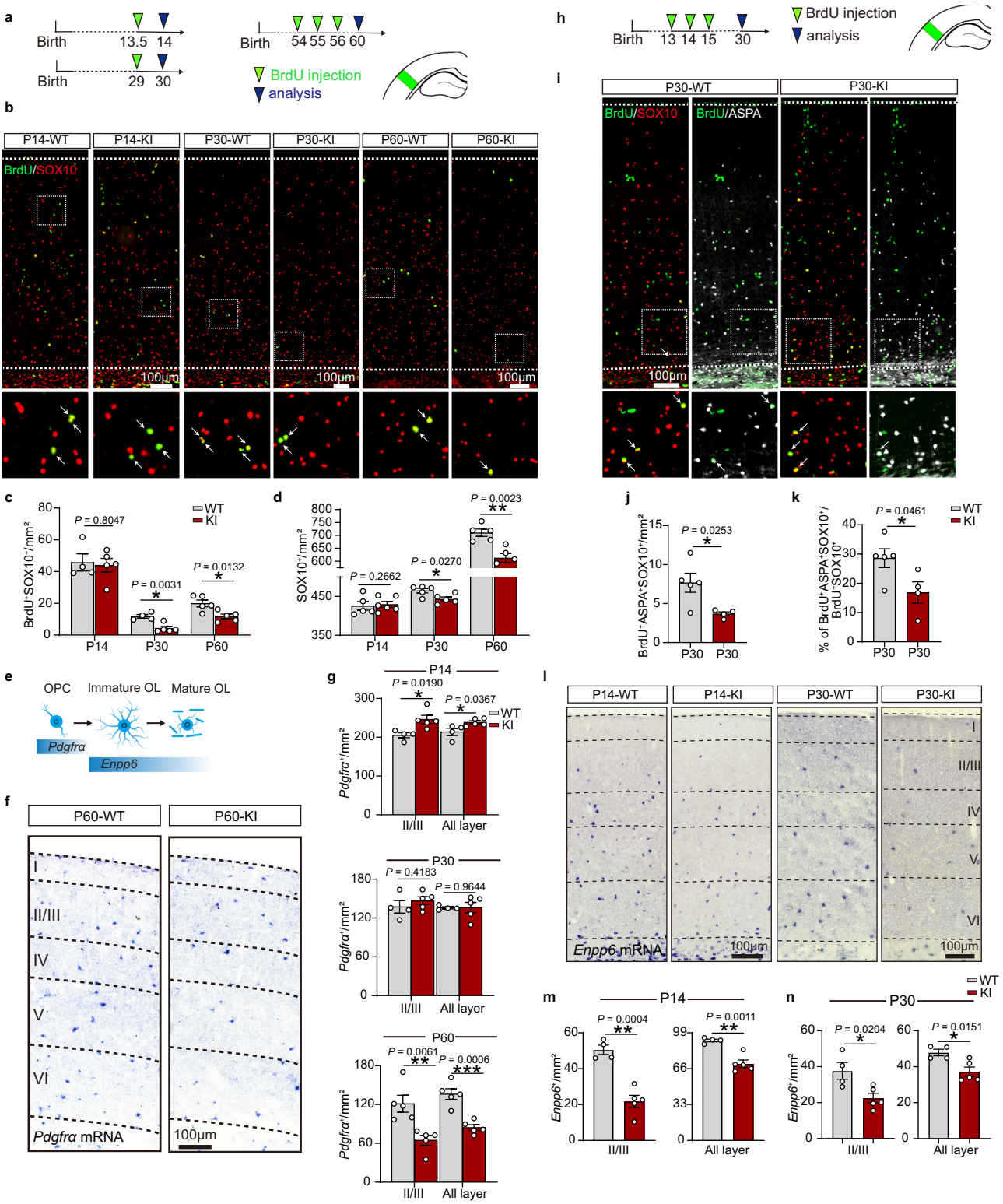

Fig. 3 | Reduced oligodendrocyte lineage proliferation and differentiation in the barrel cortex of KI mice. a An experimental schedule. **b**, **c** IHC (**b**) and quantification (**c**) of OL lineage incorporated with BrdU in BC (BrdU/SOX10, green/red; P14 and P30: WT/KI = 4/5 mice; P60: $n = 5$ mice/group). **d** Quantification of SOX10$^+$ OL lineage cells at the age of P14, P30 and P60 (P14: WT/KI = 5/6 mice; P30 and P60: WT/KI = 5/5 mice). **e** OL lineage progression and expression of stage-specific markers. RNAs are indicated in italics. **f**, **g** ISH (**f**) and quantification (**g**) of *Pdgfra*$^+$ OPCs in different layers of BC at the age of P14, P30 and P60 (p14 and p30: WT/KI = 4/5 mice; p60: $n = 5$ mice/group). **h** Experimental schedule. **i**–**k** Immunostaining for BrdU, SOX10 and ASPA displaying OL lineage proliferation and differentiation in layer II/III BC at P30. Quantification of newly differentiating OL numbers (**j**), percentage composition (**k**). Brdu, green; SOX10, red; ASPA, white. WT, $n = 5$; KI, $n = 4$. **l**–**n** ISH (**l**) and quantification (**m**, **n**) of *Enpp6*$^+$ OLs in different layers of BC at the age of P14 and P30 (**m**, **n**: WT/KI = 4/5 mice). All data are shown as mean ± SEM; *P*-values were obtained by 2-tailed unpaired Student's *t*-test. Source data are provided as a Source Data file.

https://doi.org/10.1038/s41467-025-61455-0

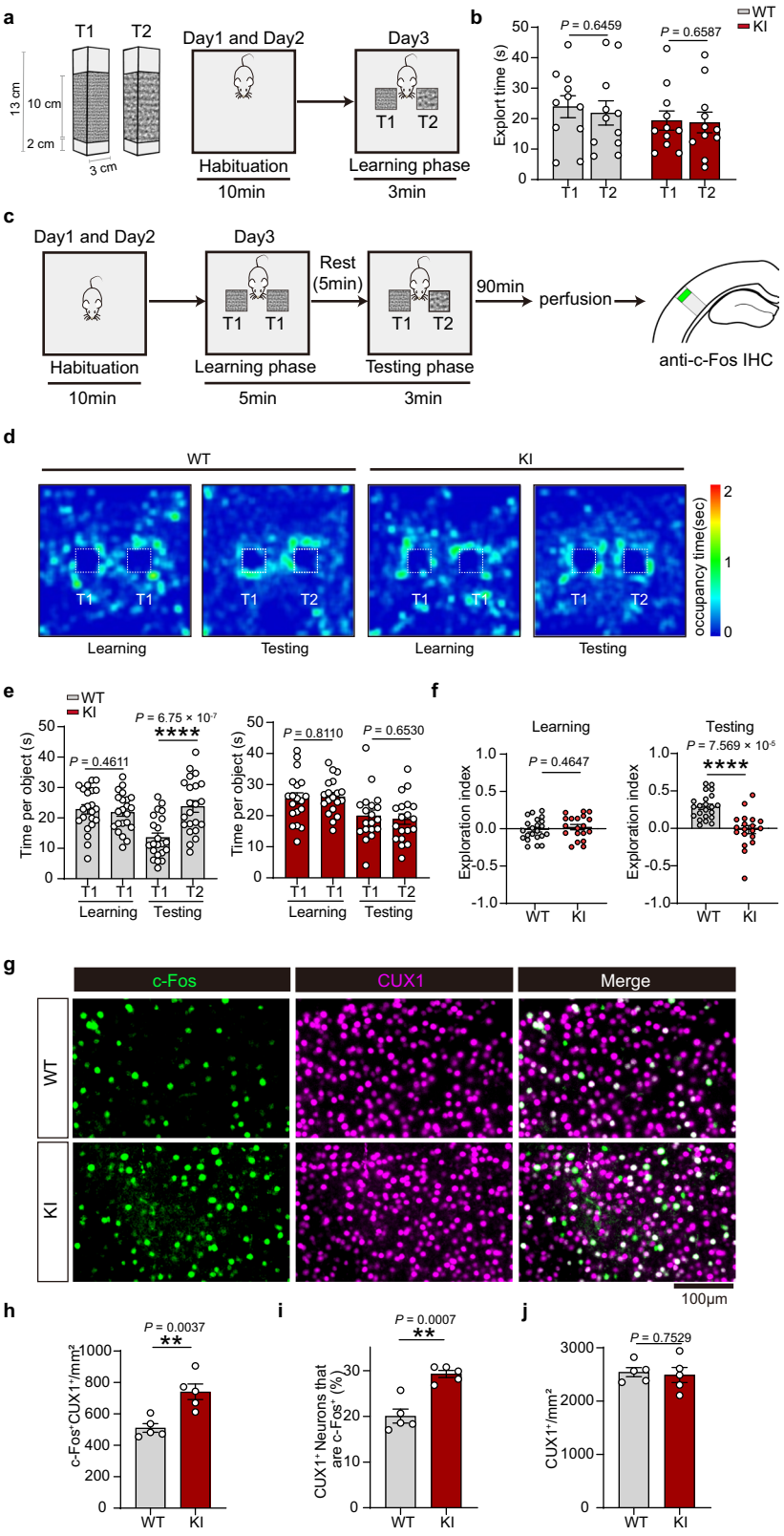

PV, or in the fluorescent area of NF200 itself (Supplementary Fig. 6g, h) at P60, which can also be seen in the immunogold EM (Fig. 6o) and EM (Fig. 2n) results and further suggesting a generally normal PV interneuron development in KI mice. As co-labeling of PV and MBP showed the total length of myelinated PV interneuron axons (Fig. 6k), we divided this by the total length of PV+ axons (Supplementary Fig. 6g) and estimated that approximately 67% of the length of all PV+ axons were myelinated in the BC (layer II/III) of WT mice at P60 (Supplementary Fig. 6i), which was also confirmed by our immunogold EM analysis (Fig. 6p), and is highly consistent with a previous report[49]. However, in the KI mice, the length of myelinated PV^+ axons was only about 29% of the total length of all PV^+ axons (Supplementary Fig. 6i, Fig. 6p), again suggesting an insufficient state of myelination of PV interneurons. As PV interneurons in layer II/III of BC receive long-range

Fig. 4 | Impaired whisker-based texture discrimination in KI mice accompanied by aberrant c-Fos hyperactivation in the layer II/III barrel cortex. a Cartoon depicting different texture roughness of the objects (Left) and a scheme of the differing textures exploration test (Right). **b** Scatter plot showing no preference for exploring textures T1 or T2 ($n = 11$ mice/group). **c** Schematic of the whisker-dependent discrimination task and experimental design to verify brain activity during texture discrimination task. 1.5 h after the end of the testing phase, mice were perfused, and their brains were subsequently removed. **d** Heat maps showing the locations of a WT mouse (left) and a KI mouse (right) in a texture discrimination task. The heat map represents the amount of time the animal spent at each location. **e** Scatter plots depicting time spent exploring identically textured objects during the learning phase and time spent exploring the novel (T2) and the familiar (T1) object for WT (left) and KI (right) groups (WT/KI = 22/19 mice). **f** Scatter plot showing exploration index for animals in (**e**). **g**–**j** IHC (CUX1/c-Fos, magenta/green) and quantification of CUX1$^+$ neurons expressing c-Fos in the BC layer II/III after texture discrimination task ($n = 5$ mice/group). Data shown as mean ± SEM. In (**e**), *P*-values were obtained by 2-tailed paired Student's *t*-test. In (**b**), (**f**), (**h**), (**i**), (**j**), *P*-values were obtained by 2-tailed unpaired Student's *t*-test. Source data are provided as a Source Data file.

excitatory inputs from the ventral posterior medial thalamic nucleus (VPM), with axons traversing from layer VI to II/III (Supplementary Fig. 6j)[50], we further assessed their sEPSCs at P60. Our results showed that both the amplitude and frequency of sEPSCs in PV interneurons remained unchanged, suggesting that long-range synaptic transmission from VPM to BC layer II/III was not affected (Supplementary Fig. 6l, m). In addition, we examined early synaptogenesis of PV interneurons at P14 and found no significant differences in the levels of VGlut1- and Homer1-positive puncta between the two genotypes (Supplementary Fig. 6o, p), suggesting that synaptogenesis of PV interneurons is also unaffected in KI mice.

Since the location of the axon initial segment (AIS) and the distribution of ion channels in the proximal axons are critical determinants of action potential threshold and firing[51,52] and are susceptible to myelin alterations[53,54], we wondered whether they would be affected by the observed hypomyelination in these PV interneurons. We examined the expression pattern of voltage-gated sodium channels (NaV) in the AIS of PV interneurons using triple staining for NaV1.6, MBP and PV (Fig. 6t). We found a significant increase in the average length of both the AIS proximal onset (Fig. 6u) and the NaV1.6 immunosignals in the AIS (Fig. 6v), as well as the distance from the soma to the onset of the first MBP signal (Fig. 6w) in PV interneurons from KI mice compared to WT controls. Interestingly, there is a strong positive correlation between the length of AIS onset and the distance to the first detectable MBP signal (Fig. 6x), while the latter is negatively correlated with the total length of PV+ myelin in the BC (layer II/III) (Fig. 6y). These results suggest that defects in myelination lead to an abnormal distribution of the NaV1.6 channels and the initial myelin sheath in the proximal axons of PV interneurons in *NL3-R451C*-KI mice, which may result in their observed reduced excitability.

We further examined the myelination level of pyramidal cell axons in the BC (layer II/III). The results showed no differences in the length of AnkG and internode myelin segment (MBP flanked by AnkG at both ends) between KI and WT mice (Supplementary Fig. 10a–d). Consistently, there were also no differences in the percentage of myelinated CUX1+ cells (Supplementary Fig. 10f) and in the tonic excitability of pyramidal cells (Supplementary Fig. 10h) or in the amplitude and frequency of mEPSCs (Supplementary Fig. 10m, n) between genotypes. These results suggest that the myelination and intrinsic properties of pyramidal cells are unaffected by the mutation.

Thus, the observed task-related overactivation of pyramidal cells in KI mice is most likely due to reduced inhibitory input from the PV interneurons, as a result of their hypomyelination state and hence reduced excitability.

Clemastine rescues PV interneuron hypomyelination and behavior deficit in KI mice

To further investigate the link between the hypomyelination of PV interneurons and their reduced excitability, disturbed gamma oscillations and the sensory dysfunction in *NL3-R451C*-KI mice, we then asked whether a promyelination strategy could rescue these abnormalities. We introduced the well-established promyelinating compound clemastine fumarate[55,56] into the *NL3-R451C*-KI mice (Fig. 7a). As expected, clemastine treatment increased the myelination level of PV interneurons in layer II/III of the BC in KI mice (Fig. 7b–e). Notably, it simultaneously restored their excitability (Fig. 7f, g). Most importantly, it rescued texture discrimination ability (Fig. 7k–m), accompanied by reduced task-related c-Fos activation of CUX1-positive pyramidal neurons (Fig. 7n–q), increased high gamma power and theta-gamma PAC strength (Fig. 7r–y). Previous RNAseq studies have shown that Chrm1, the receptor that mediates the effect of clemastine in OLs, has the highest expression in OPCs, which is approximately twice that observed in neurons, and is only expressed at low levels in microglia and astrocytes[13], the two cell types that did not appear to be affected by in vivo clemastine treatment[31]. Thus, the rescue of PV interneuron hypomyelination appears sufficient to rescue the impairment in whisker-based texture discrimination and other abnormal phenotypes in KI mice, suggesting a strong link between PV interneuron hypomyelination and sensory dysfunction.

Blocking myelination in *Myrf*-cKO mice recapitulates the PV interneuron hypomyelination and sensory deficit of *NL3* KI mice

Since the promyelinating strategy can rescue the texture discrimination dysfunction in KI mice, we next sought to further investigate whether artificially disrupting myelination would lead to a similar sensory impairment, as would be expected if there were a real link between PV interneuron hypomyelination and sensory dysfunction. To investigate this, we used the *Myrf* $^{lox/lox}$ transgenic mice, in which Cre-induced deletion of *Myrf* in OPCs and their progeny can block the production of new OLs and myelin[57]. We induced *Myrf* deletion by tamoxifen administration starting at P30, while the behavioral test was performed at P60 (Supplementary Fig. 7a). As expected, OPC-*Myrf*-cKO mice exhibited significant deficits in the overall OL and myelin production in layer II/III of the BC (Supplementary Fig. 7b–e), and in particular a reduction in the myelination level of PV interneurons (Supplementary Fig. 7h, i), while the number of PV interneurons and the total fluorescent area of PV immunolabelling remained unchanged (Supplementary Fig. 7f, g, j). Strikingly, aberrant tactile behavior similar to that seen in *NL3-R451C*-KI mice was observed in OPC-*Myrf*-cKO mice (Supplementary Fig. 7k–m), and this was also accompanied by excessive pyramidal neuron activation as seen in KI mice (Supplementary Fig. 7n–q). Thus, the blockade of overall CNS myelination, leading to BC-PV interneuron hypomyelination, is sufficient to recapitulate the sensory deficit of *NL3* KI mice, clearly demonstrating the critical link between hypomyelination and behavioral dysfunction.

OPC-*NL3*-cKO mice show decreased myelination of PV interneurons, impaired texture discrimination and dysfunctional texture-related neuronal oscillations

Given the significantly reduced NL3 immunolabelling in OPCs in *NL3-R451C*-KI mice (Fig. 1k), and given that OPCs from these mice showed impaired differentiation in vitro (Supplementary Fig. 3i), as well as the successful phenotype rescue by promyelination strategy (Fig. 7) and phenotype mimicry by myelination blockade (Supplementary Fig. 7), we finally asked whether the abnormalities observed in *NL3-R451C*-KI mice were a direct consequence of the loss of NL3 function in OPC, i.e., whether conditional deletion of NL3 specifically in OPC would also lead to abnormalities similar to those observed in KI mice.

https://doi.org/10.1038/s41467-025-61455-0

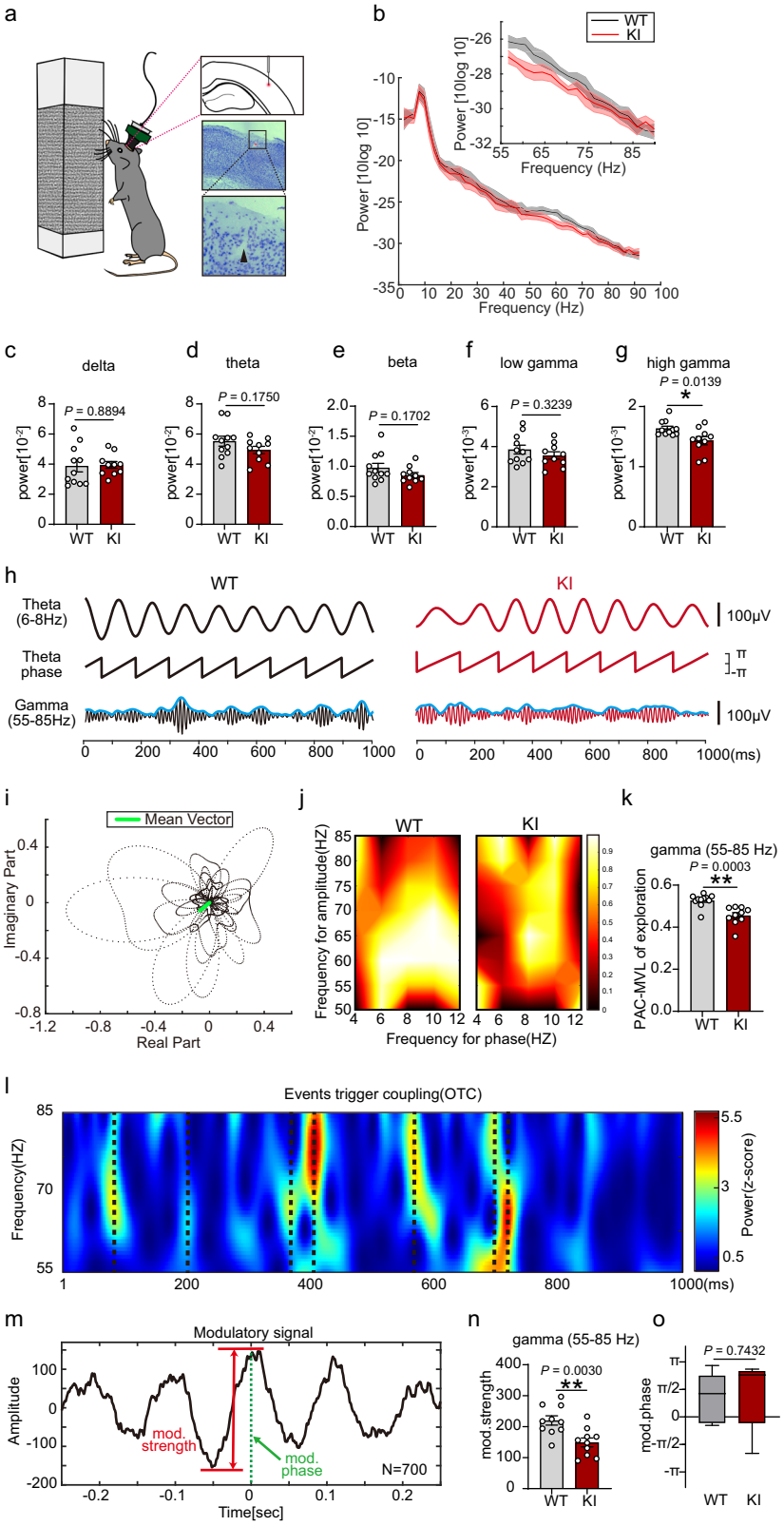

To address this question, we generated a mouse line in which *NL3* exon 6 is flanked by *loxP* sites and crossed it with *Pdgfra-CreER*^{T2} mice to yield offspring in which *NL3* was conditionally deleted in OPCs and their progeny after tamoxifen administration (OPC-*NL3*-cKO mice) (Fig. 8a, b). The efficiency of NL3 ablation in OPCs (~90% decrease in the co-localization area of NL3 with PDGFRα in *NL3*-cKO mice) was confirmed (Fig. 8c–e). Interestingly, we observed a dramatic decrease in the number of CC1^{+} mature OLs in the BC (layer II/III) of OPC-*NL3*-cKO mice at P60 (Fig. 8f, g). Concurrently, there was an overall reduction in the total length and area of MBP^{+} myelin (Fig. 8h, i) and, most importantly, a significant reduction in the total length of PV+ myelin associated with PV interneurons (Fig. 8l, m). Meanwhile, no changes were observed in the fluorescent area of PV protein (Fig. 8n) or the number of PV^{+} cells (Fig. 8j, k), suggesting that the development

Fig. 5 | Dysfunction of whisker-dependent texture-related neuronal oscillations in the layer II/III barrel cortex of KI mice. a Schematic illustration of electrophysiological recording paradigm. Black arrows highlight electrode tracks. One electrode was inserted in the BC layer II/III. The position and posture of the mouse show that the mouse is exploring the sandpaper. **b** Averaged relative BC layer II/III LFP power (1–90 Hz) when test mice explored the sandpaper (Shaded areas indicate SEM). Inset: power spectra in the 55–90 Hz range are presented to emphasize the reduction in high gamma power in KI mice. **c**–**g** Statistics of LFP power at different frequency bands. **c** Activity in the delta band (1–4 Hz); **d** activity in the theta band (4–12 Hz); **e** activity in the beta band (13–30 Hz); **f** activity in the low gamma band (30–50 Hz); **g** activity in the high gamma band (55–90 Hz) during the exploring period. WT/KI = 11/10 mice. **h** A raw signal is pass-band filtered in a low-frequency range (6–8 Hz) and the signal phase is extracted. The raw signal is also filtered in a high-frequency range (55–90 Hz), and the signal amplitude (blue curve) is extracted. **i** Example of mean vector of the composite signal (2000 sample points over a 1 s) created by the combination of the low-frequency phase and the high-frequency amplitude information. The mean vector will be non-zero and will point to the preferred phase of the modulation. The strength of the coupling corresponds directly to the MVL. **j** Standard comodulogram of PAC illustrates the modulation extent of oscillation amplitudes, ranging from 50 to 85 Hz, by the oscillation phase at frequencies ranging from 4 to 12 Hz during the exploring period. **k** Average PAC-MVL in high-frequency bands coupled to theta bands (WT/KI = 11/10 mice). **l**, **m** OTC analysis during the sniffing period in the WT. During texture discrimination behavior, an example of wavelet spectra between 55 and 85 Hz within a duration of 1 s is shown in (**l**) for illustration purposes. Summing 700 raw LFPs centered at events (black lines) identified as the large oscillations (>2 S.D. from mean power). **m** The peak-to-peak amplitude corresponds to the coupling strength (red dashed line), while the preferred phase of coupling is indicated by its phase at time 0 (green dashed line). **n**, **o** The results from employing the OTC method to measure theta-high gamma phase-amplitude coupling in identical texture discrimination test (**n**, **o**: $n = 10$ mice/group). **n** The degree of coupling aligns with conventional PAC results; **o** preferred phase of coupling. box plots show median (center line), 25th–75th percentiles (box), and min–max (whiskers). All data are shown as mean ± SEM; *P*-values were obtained by 2-tailed unpaired Student's *t*-test. Source data are provided as a Source Data file.

of PV interneurons per se remains normal in OPC-*NL3*-cKO mice. Notably, consistent with *NL3-R451C*-KI mice, there was also a significant decrease in the intrinsic excitability of BC-PV interneurons (layer II/III) in OPC-*NL3*-cKO mice in response to step-current injection compared to WT controls (Fig. 8o–q), accompanied by a decrease in both the amplitude and frequency of mIPSCs in the pyramidal neurons (Fig. 8r–t), suggesting a reduction in inhibitory synaptic transmission within local networks. Most importantly, these mice also have a similar defect in tactile discrimination (Fig. 9a–d) with excessive task-related activation of pyramidal neurons (Fig. 9e–h) as observed in *NL3-R451C*-KI mice. Unlike *NL3-R451C*-KI mice, OPC-*NL3*-cKO mice exhibited increased high gamma oscillation power (Fig. 9k), resembling PV-NMDA receptor mutants with enhanced gamma power and reduced phase-amplitude coupling[46]. The phenotypic discrepancy between these *NL3* models suggests complex underlying mechanisms requiring further investigation. However, both *NL3* models exhibited reduced theta-gamma phase-amplitude coupling (Figs. 5k, n, 9m, n). Thus, specific knockout of *NL3* in OPCs impairs BC-PV interneuron myelination and excitability, together with impaired neuronal oscillations in the BC, as well as impaired tactile sensory recognition, mimicking most of the abnormalities shown in *NL3-R451C*-KI mice and suggesting that these phenotypes are common to both *NL3* mutations.

Taken together, our results demonstrate that hypomyelination of BC-PV interneurons is closely linked to their reduced excitability, disturbed gamma oscillations, and sensory dysfunction in *NL3* mutant mice.

Discussion

In this study, we have identified a cellular phenotype—PV interneuron hypomyelination—that may underlie ASD-associated sensory dysfunction. We conducted a comprehensive survey of OL/myelin development across various brain regions at different ages in the *NL3-R451C-KI* mouse model of autism. We found a significant decrease in OL lineage cell proliferation, differentiation, and myelination capacity in the BC of KI mice, accompanied by texture recognition dysfunction and disturbed task-related pyramidal cell activity and impaired local neuronal oscillations. We further found a reduced level of myelination in BC-PV interneurons accompanied by reduced excitability in the KI mice, with their cell number and excitatory synaptic transmission remaining unchanged, whereas the myelination and intrinsic electrical properties of BC pyramidal cells are also unaffected, suggesting that the altered activation of pyramidal cells in KI mice is likely due to reduced inhibitory input from the hypomyelinated PV interneurons. Notably, these abnormalities in KI mice can be effectively rescued by a promyelinating strategy of clemastine treatment and, in contrast, recapitulated by artificial blockade of myelination in OPC-*Myrf*-cKO mice. Most importantly, conditional knockout of *NL3* in OPCs also resulted in deficits in PV interneuron myelination and excitability, as well as sensory abnormalities. These results suggest that autism-associated *NL3* mutations commonly lead to hypomyelination of the BC-PV interneuron and thereby critically contribute to sensory dysfunction.

Neuronal and synaptic plasticity mechanisms underlying ASD have been intensively studied over the past decades. Recently, a new form of brain plasticity involving OL and myelin, termed OL/myelin plasticity, has emerged as playing a critical role in various brain functions[16,22,23]. Patients with ASD often exhibit abnormal WM growth and reduced WM integrity, which are thought to contribute to core symptoms of ASD, such as atypical social communication[58]. Despite this, there is limited research directly implicating OL/myelin and/or its plasticity in ASD pathology[59]. In this context, we examined OL maturation in *NL3-R451C*-KI mice across multiple brain regions and postnatal ages and we found a significantly reduced number of mature OLs in the BC (Fig. 2b, d), but not in the mPFC, hippocampal CA1 (except at P30), or corpus callosum (Supplementary Fig. 1b, d). Interestingly, there was a long-lasting reduction in the number of OLs (Fig. 2a–d; Supplementary Fig. 4f) and a persistent impairment in the proliferation and/or differentiation capacity of OL lineage cells in the BC (Fig. 3c, k, m, n; Supplementary Fig. 4c–e), suggesting that the observed insufficient myelination (Fig. 2e–n) is not a consequence of developmental delay, but rather implies a general myelination defect in this brain area in KI mice, although the normal capacity for new OL/myelin generation continues to decline with age throughout the brain[16,60]. Why the barrel cortex appears to be the brain region most susceptible to OL dynamics changes affected by *NL3* is an interesting issue. It may be a combination of several complex factors, including the different neural circuit activities and associated rates of OL maturation and myelination between different brain regions during development[60–62], as well as the intrinsic regional heterogeneity of OPC functions per se[63].

Current research into the excitatory/inhibitory (E/I) imbalance in ASD primarily focuses on synaptic dysfunction and associated gene mutations for direct effects on neurons[64], with little attention to the role of OL/myelin and their potential contribution to this imbalance. Neuronal synchronization in the gamma frequency range is critical for the maintenance of E/I balance[10] and relies heavily on PV interneuron activity[5,65]. Meanwhile, neuronal abnormalities in PV interneurons and the consequent impaired gamma oscillations have been shown in ASD in brain regions such as the mPFC[6,7]. It has been reported that PV interneurons are the most heavily myelinated neurons in the mouse neocortex, and these in the barrel cortex have the highest degree of myelination (with half of the myelin in layer II/III observed to wrap

https://doi.org/10.1038/s41467-025-61455-0

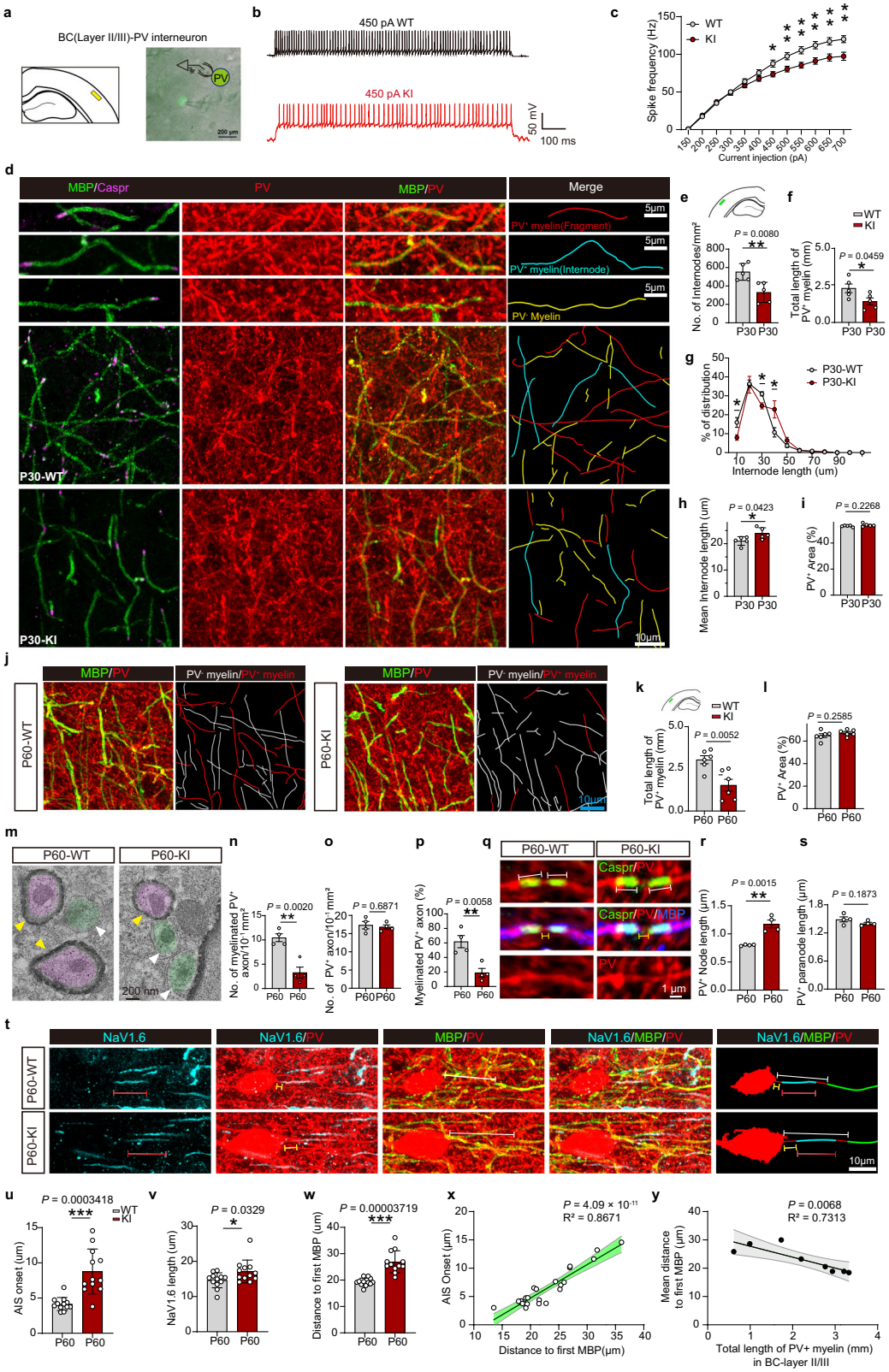

around PV interneurons) compared to the mPFC and hippocampal CA1[18,48]. Thus, an impairment of PV myelination would most likely affect their function and lead to E/I imbalance and associated behavioral dysfunction[21]. Consistently, our data revealed an overall insufficient level of myelination in layer II/III of the BC in KI mice (Fig. 2e–n). Most intriguingly, there was a dramatic hypomyelination of the PV interneurons (Fig. 6d–p), whose reduction in myelin length (~1.561 mm, Fig. 2f) accounted for more than half of the total myelin reduction (~2.930 mm, Fig. 6k) in this area, suggesting that PV interneurons may be the most severely affected neurons in the KI mice and therefore, promyelinating strategies, such as clemastine treatment, may have a more pronounced functional effect on them. Against the background of the impaired OL production and insufficient myelination in the BC, we further identified a previously unreported sensory impairment in

Fig. 6 | Reduced excitability and myelination of layer II/III PV⁺ interneurons in the barrel cortex of KI mice. a The scheme of analyzed brain region (green); right, bright field and fluorescent images of the recorded PV⁺ interneuron. **b** Representative traces of action potential firing in response to a 450-pA current step from PV⁺ interneurons in 60- to 70-day-old WT G and KI G mice. **c** Histogram of firing frequency (spikes/s) revealed differences from 150 pA to 700 pA (15 neurons/group from 4 mice). $P = 0.02358/0.009065/0.00356/0.003178/0.003789/0.003565$ at 450–700 pA. **d** Representative confocal magnified images of myelinated PV⁺ axons (upper) immunostained for MBP (green), caspr (magenta) and PV (red). Detailed view of representative subregions of a single section in layer II/III BC (lower) of WT and KI mice at P30. Red lines: Traces of PV⁺ myelin fragments; Cyan lines: Traces of PV⁺ internodes; Yellow lines: Traces of PV⁻ myelin. **e**–**i** Quantitative analysis of mean PV⁺ axon internodes number (**e**), total PV⁺ myelin length (**f**), PV⁺ axon internodes length (**g**), mean PV⁺ axon internodes length (**h**), and PV⁺ immunostaining area (**i**) in layer II/III BC at P30 ($n = 5$ mice/group). In (**g**), $P = 0.02749/0.9219/0.01195/0.046991$ at 10–40 µm. **j**–**l** Detailed view of representative subregions (**j**) of a single section in layer II/III BC of adult (P60) in WT and KI mice. MBP, green; PV, red. Red lines: Traces of PV⁺ myelin; White lines: Traces of PV-myelin. Quantitative analysis of total PV⁺ myelin length (**k**) and PV⁺ immunostaining area (**l**) in layer II/III BC ($n = 6$ mice/group). **m** Immunoelectron microscopy micrographs of myelin in layer II/III of BC (cross-sectional orientation, see Fig. 2i) in WT and KI mice. **n**–**p** Quantification of the density of PV+ immunogold-labeled myelinated axons (**n**), indicated by false-colored magenta/yellow arrows in (**m**); PV+ immunogold-labeled axons (**o**), indicated by false-colored green/white arrows in (**m**); and the proportion of myelinated PV+ axons (**p**). $n = 4$ mice/group. **q**–**s** Representative confocal images of single nodes of Ranvier flanked by Caspr (green) expressing paranodes of PV+ (red) axons labeled MBP (blue) in WT and KI mice BC layer II/III at P60. Quantitative analysis of node length (**r**) and paranode length (**s**) in BC layer II/III at P60 ($n = 4$ mice/group). **t** Confocal magnified images of PV⁺ axons immunostained for MBP (green), NaV1.6 (cyan) and PV (red). The NaV1.6 channel length (red lines), AIS onset length (yellow lines) and distance to the first MBP signal (white lines) are indicated. **u**–**w** Dot plot of the AIS onset length (**u**), NaV1.6 channel length (**v**), and distances from the soma edge to the first MBP signal (**w**) in layer II/III BC at P60 (12 neurons/group from 4 mice). **x** The correlation between AIS onset length and distances to the first MBP signal (24 neurons combined from 4 WT and 4 KI mice). **y** The correlation between the PV+ myelin length per mm² and distances to the first MBP signal ($n = 8$ mice combined from 4 WT and 4 KI; 3 neurons per mouse for the first MBP distance measurements, averaged; 9 fields per mouse for PV⁺ myelin length measurements, averaged). All data are shown as mean ± SEM. In (**c**), (**e**), (**f**), (**h**), (**i**), (**k**), (**l**), (**n**–**p**), (**r**), (**s**), and (**u**–**w**), statistical analyses were evaluated with 2-tailed unpaired Student's *t*-test. (**g**) was evaluated with two-way ANOVA and Bonferroni's multiple-comparisons test. In (**x**) and (**y**), lines represent linear regression (mean prediction), and the shaded area represents 95% CI. Pearson correlation analysis. Source data are provided as a Source Data file.

tactile texture discrimination (Fig. 4a–f) in the *NL3-R451C*-KI mice. Since sensory dysfunctions have been frequently reported in other ASD models and 90% of ASD individuals suffer from symptoms of sensory abnormalities[2,66–68], this finding in *NL3* mutant mice would provide a useful behavioral paradigm for related studies in the future. In addition to the hypomyelination of PV interneurons, our result further revealed a number of myelin-associated abnormalities, including increases in the AIS onset length, NaV1.6 channel length, and the distances from the soma edge to the first MBP signal in their proximal axons (Fig. 6u–y). Previous research showed that stimulation of PV interneurons initiates gamma rhythm and modulates sensory responses[65]. Concurrently, PV interneuron firing at theta-nested gamma frequency facilitates the coordination between theta and gamma rhythms[10]. Notably, the start and end position of the AIS correlates positively with threshold current density[51], suggesting that the location of the AIS is a critical determinant of the action potential voltage threshold and firing characteristics of individual neurons. Thus, the observed impairments in myelination and other myelin-associated defects in PV interneurons could independently contribute to E/I imbalance by reducing PV interneuron excitability (Fig. 6c). This reduction likely affects their inhibitory synaptic transmission to pyramidal neurons (Supplementary Fig. 10i–k), leading to the overactivation of these pyramidal neurons (Fig. 4h, i). Consequently, this disruption results in impaired gamma oscillations (Fig. 5g, k, n) and, ultimately, sensory dysfunction in the KI mice. Notably, the number and excitatory synaptic transmission of PV interneurons (Supplementary Fig. 6i–m), as well as the intrinsic electrophysiological properties of pyramidal neurons (Supplementary Fig. 10g–n), appear to remain unchanged. Interestingly, the hypomyelination of PV interneurons and the sensory deficits in KI mice could be simultaneously and effectively rescued by a promyelinating strategy of clemastine treatment (Fig. 7) and, in contrast, recapitulated by artificial blockade of myelination in *OPC-Myrf*-cKO mice, further suggesting that myelination deficits in PV interneurons critically contribute to the sensory dysfunction in this ASD mouse model.

There are few reports on the regulation of myelin development by autism-associated gene mutations. While the role of NL3 in neurons is well documented[3,8–10,69,70], its involvement in OL/myelin development remains largely unknown[71]. Our data show that NL3 is well expressed in all OL lineage cells both in vitro and in vivo (Fig. 1) and that there is impaired OL/myelin production in vivo in the BC of both *NL3-R451C*-KI mice (Fig. 2f) and OPC-*NL3*-cKO mice (Fig. 8i), as well as an impaired in vitro OL maturation of OPCs from KI mice (Supplementary Fig. 3k, l), providing evidence for a critical role of *NL3* in OL/myelin development. The generation of *NL3* conditional KO mice and the series of KI-like abnormalities shown in these mice, including the hypomyelination of BC-PV interneurons and impaired texture discrimination ability, further suggest a direct role of NL3 in the OPC for the OL/myelin-related mechanism underlying sensory dysfunction in KI mice. However, the detailed mechanism underlying the effect of NL3 on the OPC remains to be elucidated, but it may be as follows. First, OPCs are reported form functional synapses with neurons[72] and express functional AMPA and $GABA_A$ receptors, both of which are reported to play a critical role in regulating their proliferation and differentiation[72–74]. As OPCs also express scaffolding proteins such as PSD95 and gephyrin trimer, similar to neurons[75], NL3 in OPCs may bind to these scaffolding proteins through its C-terminal PDZ domain, thereby anchoring AMPARs and GABAARs and affecting their signaling strength to regulate OL lineage cell development. Second, NL3 in OPCs/OLs may also interact with neurexin on neuronal axons to guide OPC migration and axon recognition and facilitate myelination.

In conclusion, our results demonstrate a critical role for NL3 in OL/myelin development, whose mutations commonly result in hypomyelination and reduced excitability of BC-PV interneurons, as well as impaired gamma neuronal oscillation, contributing to tactile discrimination dysfunction. Our study provides a detailed myelin-related mechanism that may be involved in the pathophysiology of ASD and highlights OL/myelin as potential therapeutic targets for this disease.

Methods

Ethics statement

All animal procedures were conducted with the approval of the Scientific Research Animal Ethics Committee of South China Normal University (ethics approval number: SCNU-BRR-2021-022) and adhered to the US National Institutes of Health Guidelines for the Care and Use of Laboratory Animals.

Animals

The *NL3-R451C*-KI-G mice were obtained by crossing *NL3-R451C*-KI mice (129; C57BL/6)[33] with G42 mice (C57BL/6)[76], two previously described mouse lines[10]. For conditional knockout (cKO) of *NL3* in OPCs, *Pdgfra-CreER^{T2}* mice (predominantly C57BL/6)[29,77] were crossed with *NL3^{lox}* mice (C57BL/6, Cat#: S-CKO-08679, Cyagen Biosciences, Inc., Guangzhou, China), which had exon 6 of *NL3* flanked by *loxP* sites. Mice with the genotype *Pdgfra-CreER^{T2};NL3$^{lox/lox}$* were designated as *NL3*

https://doi.org/10.1038/s41467-025-61455-0

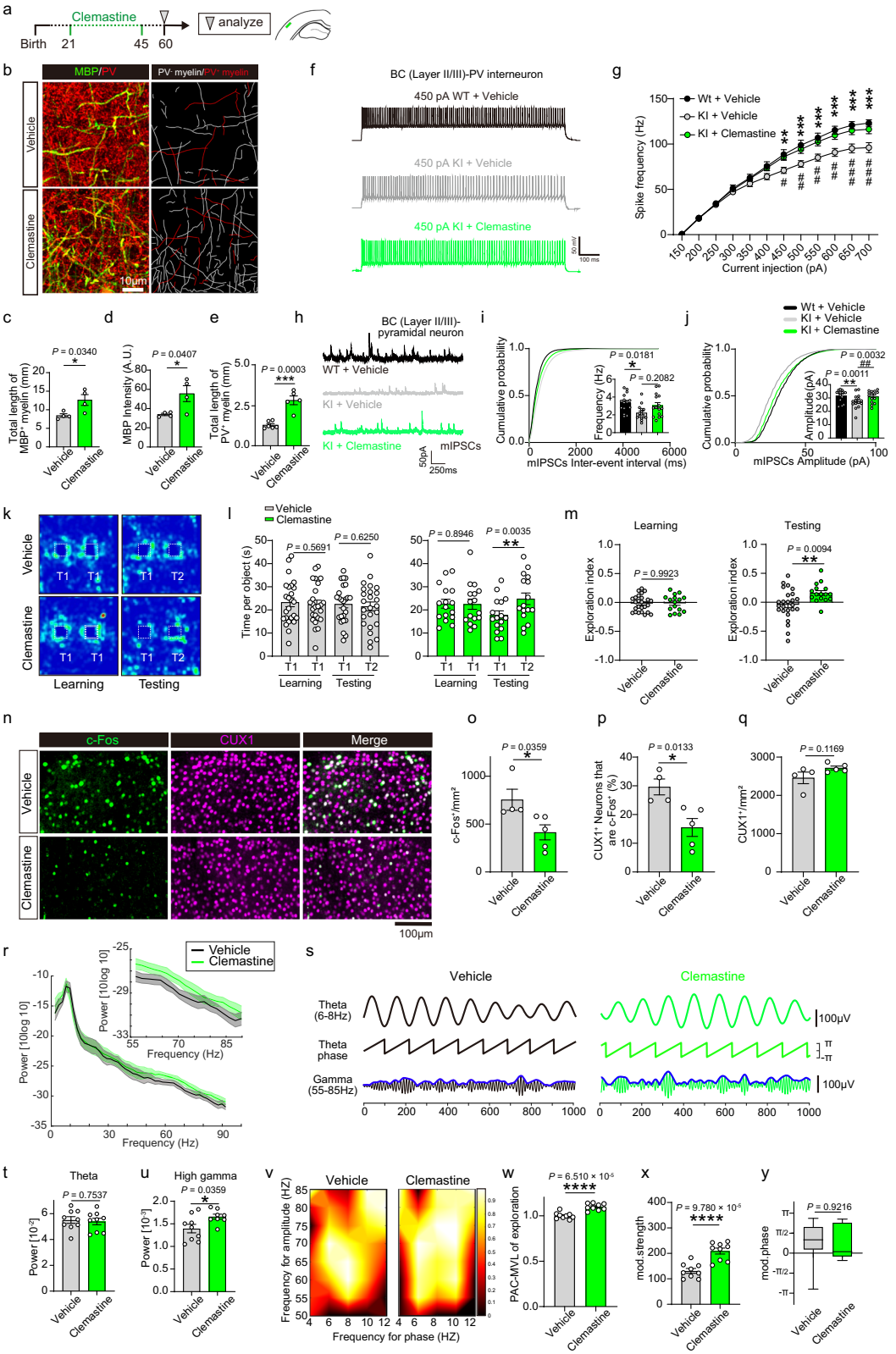

cKO, while *NL3*$^{lox/lox}$ littermates served as controls following tamoxifen administration. *Myrf*$^{lox/lox}$ mice[29,78] were crossed to the *Pdgfra-CreER*^{T2} line to generate *Myrf*$^{lox/lox}$*; Pdgfra-CreER*^{T2} offspring (mixed C57BL/6, CBA, 129 genetic background – mainly C57BL/6, although coat color was agouti, hence CBA-derived). These lines were maintained through crosses of *Myrf*$^{lox/lox}$; *Pdgfra-CreER*^{T2} and *Myrf*$^{lox/lox}$ breeders, generating *Myrf*$^{lox/lox}$*;Pdgfra-CreER*^{T2} (*Myrf*-cKO) and *Myrf*$^{lox/lox}$ control littermates. The *NL3* gene is located on the X chromosome, and a previous report indicated that heterozygous females carrying the mutation are not typically affected individuals[79]. To ensure consistency in the phenotypic analyses, we focused our experiments on male offspring. Male mice were exclusively employed in all experimental procedures. Mice were housed in a controlled environment with a 12-h light/dark cycle, at a temperature of 22–25 °C and 40–60% humidity,

Fig. 7 | Clemastine improves PV interneuron myelination and excitability, as well as tactile behavior and neuronal oscillations in KI mice. a An experimental schedule. **b**–**e** Detailed view of representative subregions (**b**) of a single section in layer II/III BC of adult (P60) in vehicle-treated KI mice and clemastine-treated KI mice (MBP/PV, green/red). Red lines: Traces of PV^+ myelin; White lines: Traces of PV-myelin. Quantitative analysis of MBP length (**c**) and density (**d**), total PV^+ myelin length (**e**) in layer II/III BC. In (**c**) and (**d**), $n = 4$ mice/group. In (**e**), WT/KI = 6/5 mice. **f** Representative traces of action potential firing responses to a 450-pA current step from PV^+ interneurons in 60- to 70-day-old mice. **g** Histogram of firing frequency (spikes/s) revealed differences from 150 pA to 700 pA (115 neurons/group from 4 mice). * denotes a significant difference between WT + vehicle and KI + vehicle ($P = 0.0106/0.0042/0.0020/0.0006/0.0004/0.0003$ at 450–700 pA); # indicates a difference between KI + vehicle and KI + clemastine ($P = 0.0088/0.0080/0.0070/0.0066/0.0075/0.0102$ at 450–700 pA). **h** Patch-clamp recordings of mIPSCs in pyramidal neurons of layer II/III BC. **i**–**j** Quantification of frequencies (**i**) and amplitudes (**j**) of mIPSCs (15 neurons/group from 4 mice). **k** Heat maps showing the locations of a vehicle-treated KI mouse (upper) and a clemastine-treated KI mouse (lower) in a texture discrimination task. **l** Scatter plots depicting time spent exploring identically textured objects during the learning phase and time spent exploring the novel (T2) and the familiar (T1) object for Vehicle (left) and Clemastine (right) groups (Vehicle/Clemastine = 25/16 mice). **m** Scatter plot showing exploration index for animals in (**l**); Vehicle/Clemastine = 25/16 mice. **n**–**q** IHC (CUX1/c-Fos, magenta/green) and quantification of $CUX1^+$ neurons expressing c-Fos in the BC layer II/III after texture discrimination task (Vehicle/Clemastine = 4/5 mice). **r** Averaged relative BC layer II/III LFP power (1–90 Hz) when test mice explored the sandpaper (Shaded areas indicate SEM). Inset: power spectra in the 55–90 Hz range are presented to emphasize the increase in high gamma power in clemastine-treated KI mice. **t**, **u** Statistics of LFP power at different frequency bands. **t** Activity in the theta band (4–12 Hz); **u** activity in the high gamma band (55–90 Hz) during the exploring period ($n = 9$ mice/group). **s** Theta and gamma oscillations of the original signal and the corresponding phase and amplitude. **v**, **w** Standard comodulogram of PAC (**v**). Average PAC-MVL (**w**) in high-frequency bands coupled to theta bands ($n = 9$ mice/group). **x**, **y** The results from employing the OTC method to measure theta-high gamma phase-amplitude coupling during the texture discrimination task ($n = 9$ mice/group), summing 700 raw LFPs centered at events identified as the large gamma oscillations. **x** The degree of coupling strength with the OTC method; **y** the preferred phase of coupling, box plots show median (center line), 25th–75th percentiles (box), and min–max (whiskers). All data are shown as mean ± SEM. Statistical analyses of results in (**c**), (**d**), (**e**), (**m**), (**o**), (**p**), (**q**), (**t**), (**u**), (**w**), (**x**) and (**y**) were evaluated with 2-tailed unpaired Student's *t*-test. In (**l**), *P*-values were obtained by 2-tailed paired Student's *t*-test. (**g**) was evaluated with two-way ANOVA and Bonferroni's multiple-comparisons test. Source data are provided as a Source Data file.

and were provided with unrestricted access to water and standard chow. Young adult mice (P60-70) were used for electrophysiological investigations and P60-75 mice for behavioral assays. All mice were anesthetized with 1% sodium pentobarbital, followed by transcardial perfusion with PBS and PFA for subsequent immunohistochemistry.

Administration of tamoxifen

Tamoxifen (Sigma, Cat: T5648) was dissolved in Miglyol at 10 mg/ml. Postnatal or adult mice received intraperitoneal injections of tamoxifen based on their body weight (100 mg/kg body weight). Injection time points are specified in the figures. Neonatal mice received a single intraperitoneal injection of 300 µg tamoxifen (30 mg/ml stock solution) on postnatal day 5.

Drug treatment

Clemastine (SelleckChem, Cat: S1847) was administered orally to 21-day-old *NL3-R451C*-KI mice at a dosage of 10 mg/kg/day through drinking water for 25 days. Clemastine was initially dissolved in dimethyl sulfoxide (DMSO) to achieve a concentration of 30 mg/ml, followed by further dilution in drinking water. The vehicle consisted of drinking water containing DMSO.

BrdU and EdU labeling

To examine proliferation, we administered 5-ethynyl-2′-deoxyuridine (Edu, ChemCruz, Cat: 61135-33-9) in drinking water. The EdU was dissolved in water with 0.2 mg/ml. Intake was monitored daily to assess whether consistent volumes were consumed across experiments. Bromodeoxyuridine (BrdU, Sigma, Cas: 59-14-3) was prepared as a 10 mg/ml solution in PBS and administered via intraperitoneal injections at a dose of 100 mg per kg. The timing of water intake and injections is indicated in the figures.

Tissue processing

After inducing deep anesthesia with 1% sodium pentobarbital, mice underwent transcardial perfusion with 4% paraformaldehyde in 0.1 M PB following an initial flush with 0.01 M PBS. Subsequently, brains were collected and postfixed overnight in 4% paraformaldehyde in 0.1 M PB. The brains were then dehydrated through a gradient of 20% and 30% sucrose in 0.01 M PBS. Following dehydration, the brains were embedded in optimal cutting temperature compound (SAKURA, Japan, Cas: 4583) and coronally sliced at a thickness of 20 µm using a cryostat microtome (CM 1850, Leica), collecting sections at specific coordinates relative to Bregma. Brain regions were defined using the Mouse Brain in Stereotaxic Coordinates. For instance, sections were collected at approximately 1.8 mm to 1.6 mm from Bregma for the mPFC, 0.73 mm to 0.5 mm for the corpus callosum, and −1.43 mm to 1.67 mm for the BC.

Immunofluorescence staining

For immunohistochemistry (IHC) staining, floating sections were initially blocked with 5% goat serum and 0.3% Triton X-100 for 2 h at room temperature. Subsequently, they were sequentially incubated overnight at 4 °C with primary antibodies, followed by incubation with fluorescent secondary antibodies for 2 h at room temperature. The primary and secondary antibodies were diluted in a blocking solution. For in vitro Immunocytochemistry, cells were initially fixed with 4% paraformaldehyde (PFA, Sigma, Cat: P6148) in phosphate-buffered saline (PBS) for 15 min at room temperature. Subsequently, they were blocked in PBS containing 1% bovine serum albumin (BSA) and 0.3% Triton for 30 min at room temperature. Following blocking, cells were then incubated overnight at 4 °C with the relevant primary antibody, followed by incubation with the appropriate fluorescence-conjugated secondary antibody for 1 h at room temperature. Primary antibodies include: Rabbit anti-NG2 (1:200, Abcam, Cat: AB5320); rabbit anti-NF200 (1:2000, Sigma-Aldrich, Cat: N4142); Rat anti-MBP (1:500, BioRad, Cat: MCA409S); Mouse anti-CC1 (1:500, Calbiochem, Cat: OP80); Mouse anti-Caspr (1:2000, NeuoMab; Cat:75-001); Mouse anti-NL3 (1:200, NeuoMab; Cat: N110/29); Rabbit anti-ASPA (1:200, asis Biofarm; Cat: OB-PRB037-01); Rabbit anti-PDGFα (1:200, CST; Cat: 3164S); Guinea pig anti-Sox10 (1:200, asis Biofarm; Cat: OB-PGP001-01); Guinea pig anti-c-Fos (1:200, asis Biofarm; Cat: OB-PGP080-01); Rat anti-CUX1 (1:200, asis Biofarm; Cat: OB-PRT034-01); rabbit anti-NaV1.6 antibodies (1:500, Alamone labs, Cat: ASC-009); Mouse anti-BrdU (1:200, Abcam; Cat: ab152095); Guinea pig anti-AnkG (1:200, asis Biofarm; Cat: OB-PGP110-01). Appropriate Alexa Fluor-conjugated secondary antibodies include goat anti-mouse, goat anti-rabbit, goat anti-guinea pig and goat anti-rat (1:500, Abcam). Nuclei were counterstained with DAPI (Invitrogen, Cat: D1306) at room temperature.

In situ hybridization

In situ hybridization (ISH) protocols are available at http://www.ucl.ac.uk/-ucbzwdr/Richardson.htm and in refs. 29,60. For colorimetric in situ hybridization, sections were exposed to a hybridization buffer containing a digoxigenin (DIG)-labeled complementary RNA (cRNA) probe (targeting *Pdgfrα* and *Enpp6*). Following incubation, the

https://doi.org/10.1038/s41467-025-61455-0

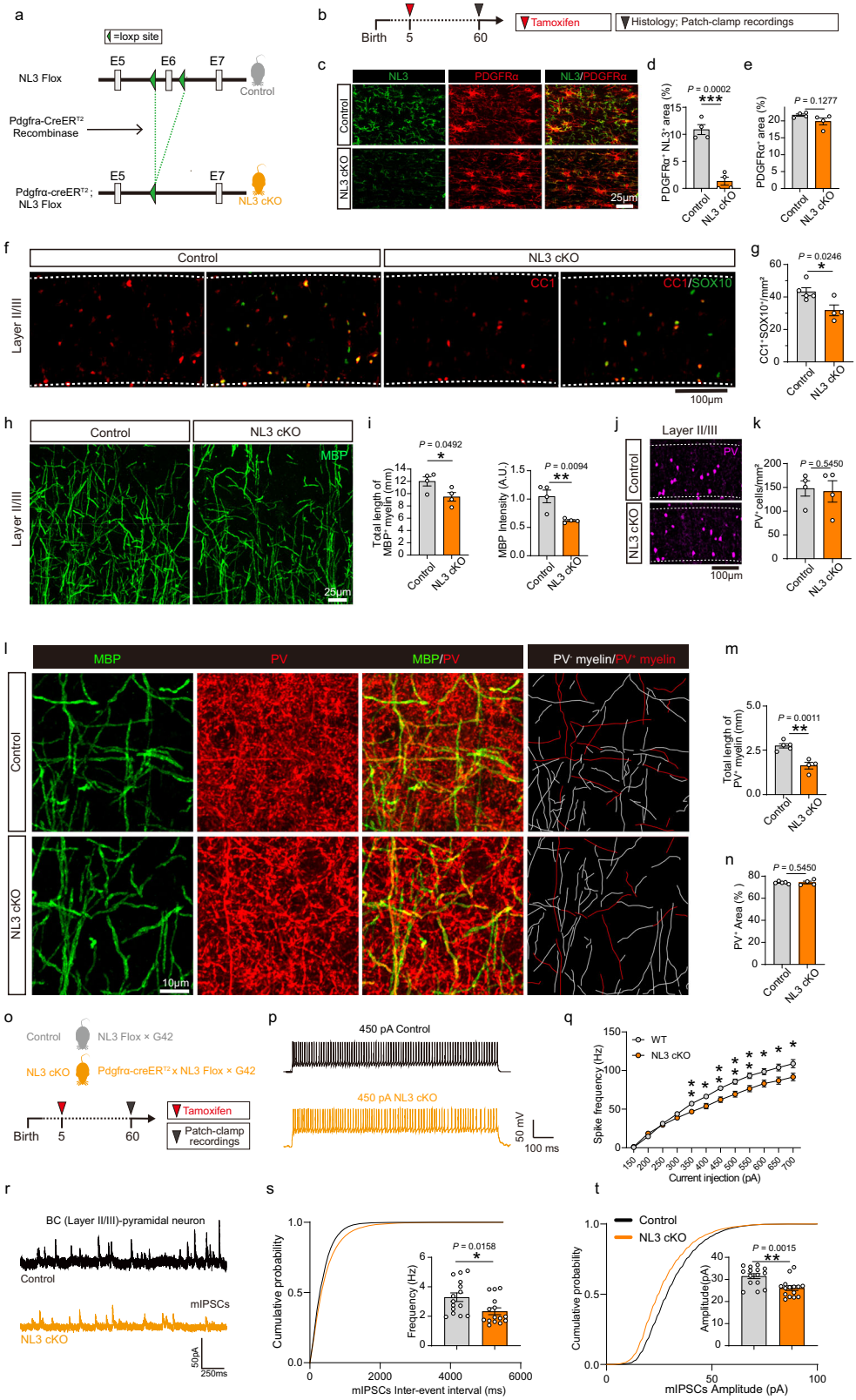

sections underwent a series of washes with buffers of varying stringency before being treated with an alkaline phosphatase-conjugated anti-DIG antibody (1:1000; Roche, Cat: 11093274910). The cRNA probes were visualized by incubating the sections with a freshly prepared colorimetric substrate solution containing NBT (nitroblue tetrazolium) and BCIP (5-bromo-4-chloro-3-indolyl phosphate) (NBT, Roche, Cat: 11383213001; BCIP, Roche, Cat: 11383221001).

Image acquisition and quantification

The brain slices and coverslips underwent scanning using the fully automated DMi8 scanner (LEICA, Germany) and LSM 900 confocal microscope (Zeiss, Jena). Signals were quantified from 3 sections per mouse at the designated Bregma position. Both the control and experimental groups were concurrently processed. Cell counts and analysis were conducted utilizing ImageJ software. Fluorescence images of Caspr,

Fig. 8 | Reduced myelination and excitability of interneurons in *OPC-NL3* cKO mice. a, **b** Illustration of the *NL3*-flox mouse line, showing that loxP sites flank exon 6. Cre-recombinase deletes exon 6 (**a**). Experimental schedule for OPC-specific and temporal control of NL3 deletion (**b**). **c**–**e** Immunostaining for NL3 (green) and PDGFRα (red) displaying the expression of NL3 in OPC (**c**). The co-localization area of NL3 and PDGFRα in *NL3* cKO mice decreased, thereby effectively producing a conditional knockout (*NL3* cKO). Quantification of NL3$^+$PDGFRα$^+$ area (**d**) and PDGFRα$^+$ area (**e**) in white matter at the age of P60 ($n = 4$ mice/group). **f**, **g** Immunostaining showing CC1 (red) co-localizing with SOX10 (green), displaying mature OLs in layer II/III BC (**f**). Quantification (**g**) of CC1$^+$ OLs in layer II/III at the age of P60 (Control/*NL3* cKO = 5/4 mice). **h**, **i** Representative IHC images (**h**) displaying MBP (green) expression in BC layer II/III at P60. Quantification (**i**) of MBP length and density in BC layer II/III ($n = 4$ mice/group). **j**, **k** IHC (PV, magenta) and quantification of PV$^+$ interneurons in layer II/III BC at the age of P60 ($n = 4$ mice/group). **l**–**n** Detailed view of representative subregions of a single section (MBP/PV, green/red) in layer II/III BC of adult (P60) in Control mice and *NL3* cKO mice (**l**). Quantitative analysis of total PV$^+$ myelin length (**m**) and PV$^+$ immunostaining area (**n**) in layer II/III BC. Control/*NL3* cKO = 5/4 mice. **o** Experimental timeline for OPC-specific and temporal control of NL3 deletion. The OPC-*NL3*-cKO mice were generated by crossing *NL3* Flox G mice (female) with *Pdgfrα*-creERT2 G mice (male). **p** Representative traces of action potential firing in response to a 450-pA current step from PV$^+$ interneurons in 60- to 70-day-old Control and *NL3* cKO mice. **q** Histogram of firing frequency (spikes/s) revealed differences from 150 pA to 700 pA (15 neurons/group from 4 mice). $P = 0.008117/0.01069/0.002376/0.002974/0.004534/0.01473/0.01289/0.02273$, at 350–700 pA. **r** Patch-clamp recordings of mIPSCs in pyramidal neurons of layer II/III of BC. **s**, **t** Quantification of frequencies (**s**) and amplitudes (**t**) of mIPSC (15 neurons/group from 4 mice). All data are shown as mean ± SEM; *P*-values were obtained by 2-tailed unpaired Student's *t*-test. Source data are provided as a Source Data file.

MBP, PV, NaV1.6, and NF200 were obtained using a ×63 objective lens (NA, 1.4) with a thickness of 15 µm. To quantify the area of fluorescent positivity and measure the length of paranodes, nodes, MBP+ myelin, PV+ myelin, and PV+ axons, three fields (each field of view measures 135.22 micrometers in both length and width) were acquired from the layer II/III of BC per brain slice, each mouse was analyzed across 9 fields of view from 3 brain sections. The regions of interest were delineated by applying a threshold set at least twice the background level.

The lengths were measured utilizing the 'straight' tool available in the Fiji software. 'total length of MBP+ myelin (mm)' and 'total length of PV+ myelin (mm)' indicated the total myelin length measured within a 0.055 mm^2 area in BC (layer II/III).

Cell counting and length measurements were conducted in a blinded manner. For cell coverslips in vitro, quantitative analysis of the results was done by counting the antigen-positive and SOX10-positive cells (total number of OL lineage cells) in at least 20 randomly selected fields per coverslip. The area occupied by MBP+ oligodendrocytes was measured using ImageJ. All cell counting and length measurements were conducted in a blinded manner.

Transmission electron microscopy and assessment of myelination

Tissue sample preparation for transmission electron microscopy was conducted following previously established protocols[80]. Briefly, mice were anesthetized with sodium pentobarbital (50 mg/kg) by intraperitoneal injection and then transcardially perfused with a solution containing 4% glutaraldehyde in 0.1 M phosphate buffer (pH 7.4). The brain tissue was harvested and fixed in 4% glutaraldehyde at 4 °C for at least one week. Afterward, a 1 mm^3 portion of the barrel cortex, marked for orientation, was dissected and fixed overnight in 4% glutaraldehyde at 4 °C. The samples underwent several washes with buffer solution, followed by post-fixation and staining steps. Dehydration was performed using increasing concentrations of acetone, followed by embedding in Epon resin and polymerization. Ultrathin sections (60 nm) were cut and stained before imaging with a transmission electron microscope.

The G-ratio was assessed using ImageJ software on transmission electron micrographs. Approximately 100–130 myelinated axons were analyzed per mouse. The myelin sheath was treated as a torus, and the areas of the inner and outer circles of the myelin sheath were determined using ImageJ's freehand tool, tracing the outer surface of each structure. These areas were then converted into hypothetical radius. The G-Ratio, representing the ratio of the diameter of the inner circle to that of the outer circle on the same myelin, was calculated. This ratio is inversely related to myelin thickness. Axon diameters were computed from their areas, also measured by tracing the outer surface of the axons. These diameters were used to create a scatter plot illustrating the relationship between axon diameter and G-Ratio, indicating a linear correlation. The frequency of myelinated axons (%) was calculated as the number of myelinated axons divided by the total number of axons, multiplied by 100. Uncompacted myelin was characterized by a wavy, loosely layered structure with visible gaps between the myelin lamellae that were markedly enlarged compared to normal compacted myelin. In contrast, myelin sheaths that appeared uniformly layered or exhibited only minor, localized loosening of the lamellae were classified as compacted myelin[80].

Immunoelectron microscopy (IEM)

Mouse cortical tissue was rapidly excised and immediately fixed in IEM fixative (Servicebio, G1124-100ML) at 4 °C. Following fixation, tissue blocks (1 mm^3) were washed three times in 0.1 M phosphate buffer (PB, pH 7.4) on ice to remove excess fixative. Next, the tissue blocks were dehydrated through graded ethanol solutions (30–100%) at −20 °C. After dehydration, resin infiltration was performed using LR White resin (HaideBio, 14381-UC) in ethanol-resin mixtures (2:1, 1:1, 1:2) for 1, 3, and 17–20 h, respectively, to allow the resin to penetrate the tissue. The samples were then embedded in pure LR White resin and polymerized under vacuum for 48 h at −20 °C using a UV polymerizer (Electron Microscopy China, UVCC2515). Subsequently, ultrathin sections (70–80 nm) were obtained using a Leica Ultra Microtome (Leica, UC7) and transferred onto 150 mesh nickel grids with formvar film (Beijing Zhongjing Keyi, BZ102615Na) for further processing. For immunolabelling, the sections were incubated with primary antibodies (PV Rabbit pAb, oasisbiofarm, OB-PRB040-01, 1:50) overnight at 4 °C. After rinsing with TBS, secondary antibodies (Anti-Rabbit IgG-Gold, Sigma, G7402, 1:50) were applied for 20 min at room temperature. The sections were then stained with 2% uranium acetate (Servicebio) for contrast enhancement before being rinsed in 70% ethanol and ultrapure water. Finally, the grids were air-dried and stored at room temperature before observation under a Transmission Electron Microscope (HITACHI HT7800/HT7700). Positive signals were identified by the presence of 10 nm gold particles.

Primary culture of mice OPC, microglia, astrocyte and neuron

All types of glial cells were purified and finally cultured in 6-well plates using a modified procedure of the reported method[81,82] for RNA extraction and qRT-PCR analysis of *NL3* expression. First, mixed glial cell cultures were prepared according to previously described rat cell cultures[81,83]. Briefly, the cortices of P0-1 mouse brains were collected in a clean 35-mm Petri dish containing cold HBSS (Gibco, Cat: 14025092) on ice to remove all meninges. Meninge-free cortices were transferred to a clean 60-mm Petri dish and minced into 1 mm^3 pieces in ice-cold HBSS, an equal volume of trypsin stock solution (0.25%, Gibco, Cat: 25200056) was added, and the tissues were then digested at 37 °C for 5 min. Digestion was terminated by the addition of complete mixed glia culture medium (MCM: DMEM + 10%FBS), followed by transfer to a 15-ml tube and gentle pipetting to release cells. The single-cell suspension was then seeded into poly-L-lysine (PLL) pre-coated 75-cm culture flasks (Corning). On the second day and the fourth day, the medium was replaced with fresh MCM. On day seven, when the mixed glial cells reached >90% confluence, the MCM medium was changed to

https://doi.org/10.1038/s41467-025-61455-0

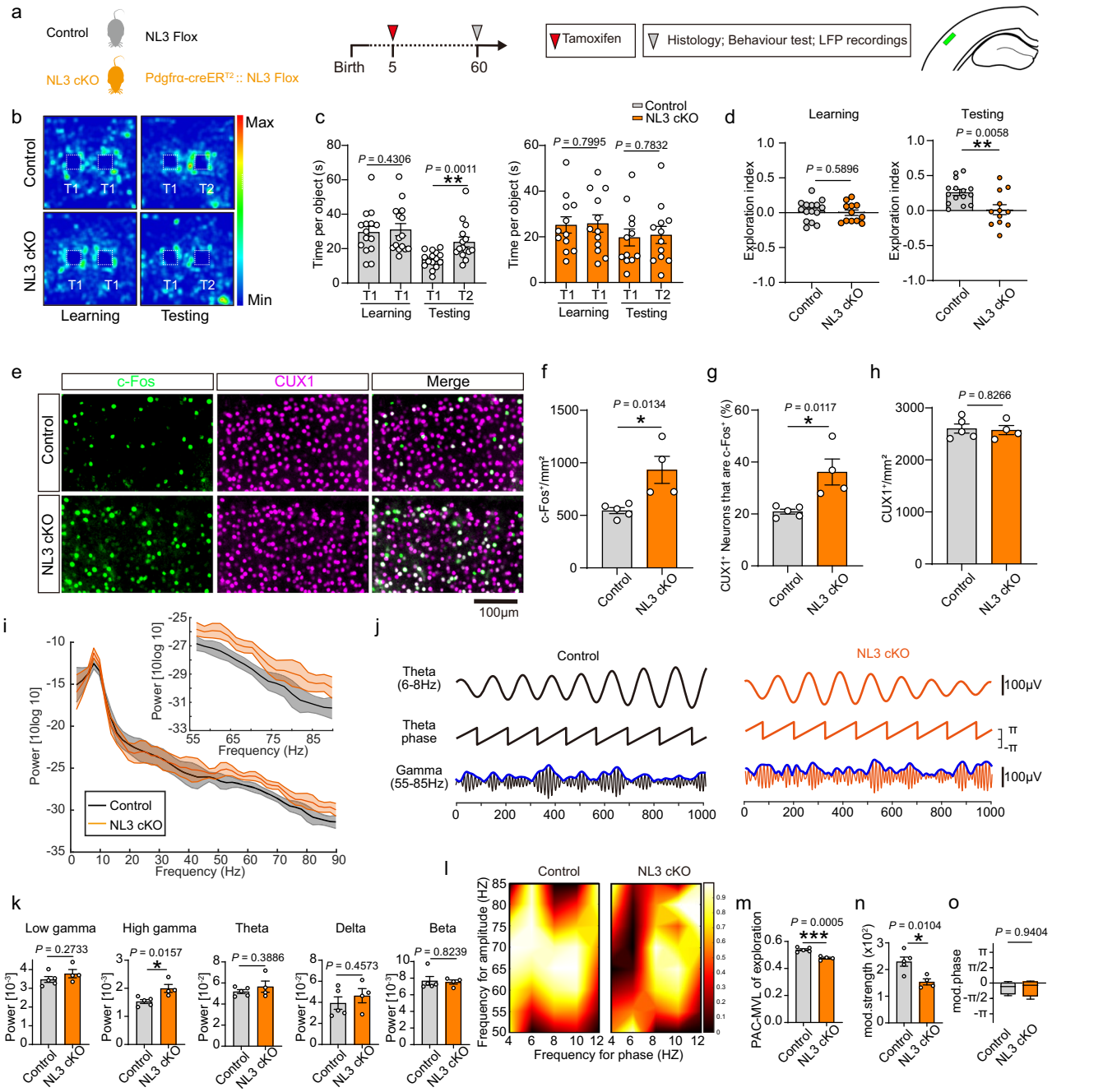

Fig. 9 | Impaired whisker-based texture discrimination and dysfunctional texture-related neuronal oscillations in the layer II/III barrel cortex of OPC-*NL3* cKO mice. a Experimental schedule. **b**, **c** Heat maps (**b**) and scatter plots (**c**) depicting time spent exploring identically textured objects during the learning phase and time spent exploring the novel (T2) and the familiar (T1) object for Control (left) and *NL3* cKO (right), Control/*NL3* cKO = 15/12 mice. **d** Scatter plot showing exploration index for animals in (**c**). Control/*NL3* cKO = 15/12 mice. **e**–**h** IHC (CUX1/c-Fos, magenta/green) and quantification of CUX1$^+$ neurons expressing c-Fos in the BC layer II/III after texture discrimination task (Control/*NL3* cKO = 5/4 mice). **i** Averaged relative BC layer II/III LFP power (1–90 Hz; Inset: 55–90 Hz) when test mice explored the sandpaper (Shaded areas indicate SEM). **j** Theta and gamma oscillations of the original signal and the corresponding phase and amplitude. **k** Statistics of LFP power at different frequency bands during the exploring period (Control/*NL3* cKO = 5/4 mice). **l**, **m** Standard comodulogram of PAC (**l**). Average PAC-MVL (**m**) in high-frequency bands coupled to theta bands (Control/*NL3* cKO = 5/4 mice). **n**, **o** The results from employing the OTC method to measure theta-high gamma phase-amplitude coupling during the texture discrimination task, summing 400 raw LFPs centered at events identified as the large gamma oscillations. **n** The degree of coupling strength; **o** preferred phase of coupling. Control/*NL3* cKO = 5/4 mice. All data are shown as mean ± SEM. Statistical analyses of results in (**d**), (**f**), (**g**), (**h**), (**k**), (**m**), (**n**) and (**o**) were evaluated with 2-tailed unpaired Student's *t*-test. Statistical analyses of results in (**c**) were evaluated with 2-tailed paired Student's *t*-test. Source data are provided as a Source Data file.

OPC proliferation medium [OPM: DMEM supplemented with 15% B104 conditioned medium, 5 µg/ml insulin (Sigma, I6634), and 1% N_2 supplement (Gibco, Cat: A1370701)] and half refreshed every day thereafter. OPCs in the upper layer reached 90% confluence by ~day 10. To isolate OPCs, microglia and astrocytes, the culture medium was removed, and OPC cell digestion solution [DPBS containing 200 µg/ml DNase I (Sigma, Cas9003-98-9), 5 µg/ml insulin, and 0.01% EDTA] was added to the flask. After ~5 min of digestion at 37 °C, the upper layer of cells containing OPCs and microglia was detached from the underlying astrocytes by gently aspirating with a flame-polished elbow glass pipette, followed by the addition of MCM to stop digestion. The cell suspension was filtered through a 70 µm filter and seeded onto an

uncoated 100-mm Petri dish (Sterilin, Staffordshire, UK) and incubated at 37 °C for 20 min to allow microglia to adhere to the bottom of the Petri dish and OPCs to remain in the suspension. OPCs in the suspension were harvested by centrifugation at approximately 175×*g* for 5 min, resuspended in OPM and then plated onto PLL-coated 6-well plates (Corning) at ~2×10^6 cells per well. OPCs were allowed to grow in OPM for 2 days before mRNA extraction, or otherwise the medium was replaced with OPC differentiation medium [ODM: Sato medium containing 15 nM T3 (Sigma, Cas: 55-06-1) + 5 μg/ml NAC (Sigma, Cas: 616-91-1) + 10 ng/ml CNTF (PeproTech, Cat: 450-13) + 15 nM NT3 (PeproTech, Cat: 450-03); Sato medium: DMEM containing 0.04 M glutamine (Gibco, Cat: 35050061), 0.1% BSA (Sigma, Cas: 9048-46-8), 0.01 M sodium pyruvate (Gibco, Cat: 1136070), 5 mg/ml insulin, 0.03 μM sodium selenite (Sigma, Cas: 10102-18-8), 50 μg/ml transferrin (Sigma, Cas: 11096-37-0), 0.01 μM dexamethasone (Sigma, Cas: 50-23-7), and 0.01 μM biotin (Sigma, Cas: 58-85-5)] on the other day after plating and allowed to differentiate for five days, with half of the ODM medium refreshed every other day to obtain mature oligodendrocytes.

Attached microglia in the Petri dish were harvested by aspiration in MCM and plated on a 6-well plate at ~2×10^6 cells per well. mRNA was extracted after 2 days. Astrocytes in the flask were washed with PBS and further digested, suspended, centrifuged, resuspended, and finally plated and allowed to grow on a 6-well plate at ~2×10^6 cells per well in MCM for 2 days before mRNA was extracted.

For the mouse neuron culture, briefly, the cortex of P0 pup was dissected and the meninges were removed in a pre-cooled HBSS and then were digested with 0.125% trypsin at 37 °C for 20 min. The digestion was then terminated with DMEM/F12 medium (Gibco, Cat: C11330500BT) containing 5% FBS (Gibco, Cat: 26140079). After centrifugation, the cells were filtered, counted and plated at a density of 1×10^6 cells per well on PLL-coated 6-well plates (Gibco, Cat: P6407) and incubated at 37 °C for at least 4 h. The medium was then replaced with Neurobasal medium (Gibco, Cat: 10888-022) supplemented with 2% B27 supplement (Gibco, Cat: 17504044) and 0.5 mM L-glutamine (Thermo Fisher Scientific, Cat: 21103049). Cells were maintained in a humidified atmosphere at 37 °C with 5% CO_2. The medium was changed every three days, and neurons were subjected to RNA extraction on day 10, with the initial plating day considered as day 0.

qRT-PCR

Different types of neural cells cultured in 6-well plates were subjected to total RNA extraction according to the manufacturer's instructions using the RNAiso Plus kit (TaKaRa, Cat: 9109). A total sampling of 6 wells for each cell type was extracted in 3 independent cultures from 3 mice. RNA quality and concentration were assessed using the Simpli-Nano spectrophotometer (GE Healthcare, Cat: 29-0617-11). Subsequently, cDNA synthesis was performed using the PrimeScript™ RT Reagent Kit (TaKaRa, Cat: RR037A) according to the manufacturer's protocol. Real-time qRT-PCR was performed using HieffTM qPCR SYBR Green Master Mix on the ABI 7500 qRT-PCR system. GAPDH was chosen as a reference gene to normalize the mRNA expression of specific genes. The $2^{-\Delta\Delta Ct}$ method was employed to calculate the relative gene expression levels based on the threshold cycle (CT) values. Primer pairs consisted of: NL3, fwd- CCAGGAGCCCAACGAAGATT and rev- GCTAAGTCCTCGCCCTGTTT; Gapdh, fwd- GTGTTCCTACCCCCAATGTGT and rev- ATTGTCATACCAGGAAATGAGCTT.

OPC culture derived from mice neurosphere progenitor cell

For the in vitro OPC differentiation study, we used a previously published neurospheres protocol[81] with some modifications as we described previously[84] (by purifying neural progenitor cells (NPCs) from the dissected cerebral cortex of WT or KI P0 mouse pups, since it is relatively time-saving). Single-cell suspensions were obtained and seeded in 6-well plates in NPC medium [DMEM/F12 (Gibco), 20 ng/ml epidermal growth factor (EGF, PeproTech, Cat: AF-100-15), 20 ng/ml basic fibroblast growth factor (bFGF, PeproTech, 100-18B-50), 2% B27 (Gibco, Cat: 17504044)][38]. NPCs were expanded as neurospheres 3 days after plating. Neurospheres were routinely passaged every 3 days. Differentiation assays were performed using neurospheres from passages 3–5. To generate OPCs, neurospheres were dissociated into single cells and seeded onto 12-mm glass coverslips (Fisher, Cat: NC1129240) coated with 0.1 mg/ml poly-D-lysine (PDL, Sigma-Aldrich, Cat: P0899), placed in 24-well plates in OPC medium [DMEM/F12 + 10 ng/ml bFGF+10 ng/ml platelet-derived growth factor (PDGF-AA, PeproTech, Cat: 315-17) + 2% B27] for a duration of 2 days. To induce OPC differentiation, the OPC medium was then replaced with differentiation medium (DMEM/F12 + 2% B27) and cultured for a further 5 days to allow OPC differentiation into MBP-positive mature oligodendrocytes. For the EdU incorporation assay to assess cell proliferation in OPC medium, cells were exposed to EdU (1 μg/ml) for 4 h. At the end of the experiments, cultured cells were finally fixed with 4% paraformaldehyde (PFA) and subjected to immunofluorescence staining.

OPC differentiation was measured by percentages of NG2+ and MBP+ cells in the culture, as well as by morphological classification and analysis of the MBP+ cells as previously described[36–38].

Behavioral assays

Behavioral tests were conducted during the light-on period of the day, utilizing age-matched male littermates. Prior to testing, mice underwent handling sessions lasting at least 2 min per day for 5 consecutive days until they became habituated to the operator.

The whisker-dependent texture discrimination task was adapted from a previously documented protocol. To promote whisker interaction, the grit (G) of the sandpaper object was selected based on previous studies[21]. A 180 G sandpaper (fine) was allocated for the familiar object (T1), while a 120 G sandpaper (coarse) was designated for the novel object (T2). Notably, both the 120 G and 180 G sandpapers shared the same color. Each mouse underwent individual habituation sessions in a 30 × 30 × 30 cm opaque plexiglass box for 10 min per day over 2 consecutive days. On the third day, designated as the testing day, the mouse was initially allowed 3 min for arena exploration (exploration phase) before being temporarily removed for less than 20 s to enable the placement of two objects (each measuring 3 × 3 ×10 cm) featuring identical textured surfaces (T1). Upon the mouse's return to the arena, it was granted 3 min to acquaint itself with the textures of the two objects (learning phase). Mice exhibiting insufficient interest in the objects (exploration time of any object less than 3 s) or displaying bias towards one object (over 60% of approaching time spent on one object) were excluded from further testing. Mice meeting the aforementioned testing criteria were temporarily removed again for 3 min to facilitate the replacement of the two objects with two new objects: one featuring the previously encountered texture and the other featuring a novel texture. The mouse was allotted 3 min to explore and interact with the new objects (testing phase). To mitigate olfactory cues, the testing arena was cleaned with 70% ethanol between sessions and between different animals. The investigation was operationally defined as the act of positioning the nose within a distance of less than 2 cm from the object or making direct contact between the nose and the object. Activities such as resting, grooming in close proximity to, or sitting on the object, were not considered instances of investigation. Additionally, the difference index was calculated as the difference in exploration time between the targets (T1 vs. T1, and T1 vs. T2), divided by the total time spent exploring both targets. Behavioral scoring was performed by an experimenter blind to the experimental conditions. Behavioral data collection and analysis were performed using the Shanghai Xinruan software (VisuTrack 3.0). In our study, a few mice in each group were excluded because they either showed insufficient exploration of the textured objects or displayed bias towards one object: 2 of 24 control and 2 of 21 KI mice, 1 of 16 control and 1 of 13 OPC-*NL3*-cKO mice, 1 of 11 control and 2 of 13 OPC-*Myrf*-cKO mice, as well as 2 of 27 vehicle group and 1 of 17 clemastine group mice.

In vivo recording

53-day-old adult mice were anesthetized with isoflurane (5% induction, 0.5–2% maintenance) and placed in a stereotaxic apparatus. Metal ground screws were then affixed above the cerebellum. Both the adult experimental group and their control littermates underwent implantation of tungsten microelectrodes (tip impedance ranging from 250 to 450 kΩ) into the left BC (1.55 mm posterior to bregma and 3.0 mm lateral to the midline). The electrodes were positioned within the superficial layer II/III, approximately 200 μm deep from the pia mater. Following the placement of electrodes, ground, and reference, dental cement was applied to firmly secure the implant to the skull. Mice were allowed a minimum recovery period of 1 week post-electrode implantation. Neuronal activity was recorded at a sampling rate of 30 kHz using the Cerebus acquisition system (Blackrock Microsystems Inc., UT). Local field potentials (LFPs) were bandpass filtered between 0.5 and 500 Hz and stored at a rate of 2000 Hz. Neurophysiological recordings were referenced to a ground wire connected to ground screws.

Power spectral density

In the power spectrum analysis, the power spectra of spontaneous LFPs for each mouse were first subjected to bandpass filtering from 1 Hz to 400 Hz using a fifth-order IIR Butterworth filter. Subsequently, line noise at 50 Hz was removed. The normalized power spectra were then calculated by computing the z-score. Employing Welch's method, MATLAB's PWELCH function was utilized to estimate the Power Spectral Density (MATLAB R2022). To mitigate spectrum leakage, the Hanning window was applied to the original signal. The power spectral density is defined as *P*. Each figure's abscissa represented frequency (*f*), while the ordinate denoted ten times the logarithm of power ($P' = 10\log_{10}(P)$).

Phase-amplitude coupling

Mean vector length. Initially, the LFP signal X(t) underwent filtration to isolate the gamma oscillation A(t) and theta oscillation B(t). Subsequently, the time oscillation phase of theta, denoted as $P_{theta}(t)$, was determined via the Hilbert transform applied to B(t).

$$\mathrm{H}[B(t)] = X_B(t) + \mathrm{i}Y_B(t) \tag{1}$$

$$\mathrm{P_{theta}(t)} = \arctan\frac{Y_B(t)}{X_B(t)} \tag{2}$$

Concurrently, the power of gamma oscillation, denoted as Agamma(t), was computed by means of a Hilbert transform applied to G(t).

$$\mathrm{H}[A(t)] = X_A(t) + \mathrm{i}Y_A(t) \tag{3}$$

$$\mathrm{Agamma(t)} = \sqrt{\left(X_{A(t)}\right)^2 + \left(Y_{A(t)}\right)^2} \tag{4}$$

Formed by the theta phase as the x-coordinate and the gamma amplitude as the y-coordinate, the mean vector represents a composite two-dimensional time series. A scatter plot of these mean vectors reveals the preferred phase of modulation, expressed as

$$z(t) = \mathrm{Agamma(t)}^* \cos\left[\mathrm{Ptheta(t)}\right] + \mathrm{i}^*\mathrm{Agamma(t)}^* \sin\left[\mathrm{Ptheta(t)}\right] \tag{5}$$

The strength of the coupling is indicated by the mean vector length. To eliminate variations stemming from amplitude differences between groups, a normalization process was applied following the construction of a random distribution based on each set of original data:

$$\mathrm{MVL_{norm}} = \frac{\mathrm{MVL_{raw}} - \mu}{\sigma} \tag{6}$$

where μ and σ represent the mean and standard deviation derived from the null distribution.

The specific scripts used for this process, implemented in MATLAB R2022, are detailed below:

```
%% compute surrogate values
npnts = length(LFP);
for bi=1: numsurrogate
cutpoint = randsample(round(npnts/10):round(npnts*.9),1);
surrogate_m(bi) = abs(mean(amplit([cutpoint:end 1:cutpoint-1]).*exp(1i*phase)));
end;
%% fit Gaussian to surrogate data
surrogate_mean = mean(surrogate_m);
surrogate_std = std(surrogate_m);
%% normalize length using surrogate data (z-score)
m_norm_length= (abs(m_raw)-surrogate_mean)/surrogate_std;
m_norm_phase = angle(m_raw);
m_norm = m_norm_length.* exp(1i * m_norm_phase);
```

Oscillation-triggered coupling

Due to the inherent limitations in temporal resolution associated with the PAC-MVL comodulogram, an alternative method known as the oscillation-triggered comodulogram (OTCG) was employed. This approach, characterized by its event-driven nature and lack of reliance on specific parameters, effectively illustrates the modulatory phase across various frequency bands. The OTC algorithm involves converting the LFP signal into a time-frequency representation through a process of convolution. This convolution entails applying a set of frequency-tailored Morlet wavelets to the LFP signal s(t), followed by a squaring operation, as exemplified by the equation:

$$E_{(t,f_0)} = \left|\mathrm{w}(t,f_0)^* s(t)\right|^2 \tag{7}$$

The symbol * denotes the convolution operation. The Morlet wavelet is characterized by the following definition:

$$\mathrm{w}(t,f_0) = A\exp\left(-t^2\sigma_t^2\right)\exp\left(2\mathrm{i}\pi f_0 t\right) \tag{8}$$

where $\sigma_f = \frac{1}{2\pi\sigma_t}$ (with σ_t and σ_f representing the standard deviations in the time and frequency domains, respectively), and the normalization factor $A = \left(\sigma_t\sqrt{\pi}\right)^{1/2}$, $f_0/\sigma_f = 8$. We select only those events with higher power (>2 S.D. from mean power) in the band of interest. The modulatory signal s is then defined as

$$s = \sum_{n=1}^{N} x(n - T \ldots n + T) \tag{9}$$

where $n = 1,\ldots, N$ represents the time stamps of the selected power peaks within the band of interest, and T represents the time window centered around each time stamp, which is included in the summation.

Slice cultures and electrophysiology

Coronal slices (300 μm) of the S1BF were prepared from two-month-old mice using a vibratome (Vibratome T1200S, Leica) in ice-cold dissection buffer containing (in mM): 212.7 sucrose, 3 KCl, 1.25 NaH_2PO_4, 3 $MgCl_2$, 1 $CaCl_2$, 26 $NaHCO_3$, and 10 dextrose, bubbled with 95% O_2/5% CO_2. Brain slices were transferred to artificial cerebrospinal fluid (ACSF) and incubated at 34 °C for 1 h. The ACSF was similar to that of the dissection buffer except that sucrose was replaced by 124 mM NaCl, and the concentrations of $MgCl_2$ and $CaCl_2$ were adjusted to 1 mM and 2 mM, respectively. All solutions were saturated with 95% oxygen and 5% carbon dioxide.

For mIPSCs, recordings were made from L2/3 pyramidal neurons of S1BF at a holding potential of −70 mV in ACSF containing tetrodotoxin (TTX; 1 μM, Sigma), AP-V (50 μM, Sigma), and CNQX (20 μM, Sigma). Patch pipettes (2–4 MΩ) were filled with the internal solution consisting of the following (in mM): 120 Cs-methylsulfonate, 10 HEPES,

10 Na-phosphocreatine, 5 lidocaine N-ethyl bromide (QX-314), 4 ATP, 0.5 GTP, pH 7.2–7.3. For mEPSCs, recordings were made from pyramidal neurons in L2/3 of S1BF at a holding potential of −70 mV. The bath solution contained TTX (1 µM, Sigma), bicuculline (20 µM, Sigma), and AP-V (100 µM, Sigma). For sEPSCs, recordings were obtained from L2/3 PV-neurons in ACSF with bicuculline (20 µM, Sigma) and AP-V (100 µM, Sigma), without TTX, to preserve spontaneous activity. For action potentials (APs) measurement, series depolarization currents were injected into neurons. APs of PV or pyramidal neurons in L2/3 of S1BF were recorded under current clamp with a pipette containing (in mM): 130 K-gluconate, 10 KCl, 10 HEPES, 0.5 Na_3GTP_4, MgATP, and 10 Na-phosphocreatine. Data were acquired after low-pass filtering at 2 kHz and digitized at 10 kHz using a Sutter amplifier. The series resistance (Rs) was <20 MΩ, and an input resistance >100 MΩ was studied.

Statistics

Before conducting any statistical analyses, the data underwent two preliminary checks. First, normality of data distribution was assessed using the Kolmogorov–Smirnov and Shapiro-Wilk tests. Additionally, outlier detection was guided by the ROUT method with a significance level set at 1% (Q = 1%), in combination with biological criteria based on prior literature and expected physiological variability. Any outliers identified were subsequently removed from the dataset prior to statistical analysis. For datasets that exhibited a normal distribution, several parametric tests were utilized, including unpaired *t*-tests, paired *t*-tests (for behavioral studies), one-way ANOVA, and two-way ANOVA. Bonferroni's post hoc tests were conducted following two-way ANOVA to make pairwise comparisons between genotypes at specific time points. Non-normally distributed datasets were subjected to the Mann–Whitney test. The significance levels (*P*-values) derived from these analyses are provided within the figures and their corresponding legends, and symbolic representations are utilized to convey different ranges of *P*-values: $P > 0.05$, $^{*}P < 0.05$, $^{**}P < 0.01$, $^{***}P < 0.001$ and $^{****}P < 0.0001$. In the case of in vivo experiments, each data point represents measurements obtained from a single mouse (excluding electrophysiology experiments), with the total number of mice included indicated in the figure legends. For electrophysiology data, each data point corresponds to a single cell, and both the number of cells and mice are specified in the figure legends. Data presentation adhered to the convention of representing the mean along with the standard error of the mean (Mean ± SEM), except for violin plots where the median and quartiles are depicted as thick and thin dashed lines, respectively. Detailed statistical parameters, including mean values, standard errors of mean, sample sizes (*n*), test statistics, and *P*-values, are provided in Supplementary Table 1.

Reporting summary

Further information on research design is available in the Nature Portfolio Reporting Summary linked to this article.

Data availability

Further data to support the findings can be obtained upon request from the corresponding authors. Source data are provided with this paper.

References

1. Carlisi, C. O. et al. Comparative multimodal meta-analysis of structural and functional brain abnormalities in autism spectrum disorder and obsessive-compulsive disorder. *Biol. Psychiatry* **82**, 83–102 (2017).
2. First, M. B. Diagnostic and statistical manual of mental disorders, 5th edition, and clinical utility. *J. Nerv. Ment. Dis.* **201**, 727–729 (2013).
3. Foldy, C., Malenka, R. C. & Sudhof, T. C. Autism-associated neuroligin-3 mutations commonly disrupt tonic endocannabinoid signaling. *Neuron* **78**, 498–509 (2013).
4. Gogolla, N. et al. Common circuit defect of excitatory-inhibitory balance in mouse models of autism. *J. Neurodev. Disord.* **1**, 172–181 (2009).
5. Buzsáki, G. & Wang, X.-J. Mechanisms of gamma oscillations. *Annu. Rev. Neurosci.* **35**, 203–225 (2012).
6. Rojas, D. C. & Wilson, L. B. γ-band abnormalities as markers of autism spectrum disorders. *Biomark. Med.* **8**, 353–368 (2014).
7. Yizhar, O. et al. Neocortical excitation/inhibition balance in information processing and social dysfunction. *Nature* **477**, 171–178 (2011).
8. Etherton, M. et al. Autism-linked neuroligin-3 R451C mutation differentially alters hippocampal and cortical synaptic function. *Proc. Natl. Acad. Sci. USA* **108**, 13764–13769 (2011).
9. Rothwell, P. E. et al. Autism-associated neuroligin-3 mutations commonly impair striatal circuits to boost repetitive behaviors. *Cell* **158**, 198–212 (2014).
10. Cao, W. et al. Gamma oscillation dysfunction in mPFC leads to social deficits in neuroligin 3 R451C knockin mice. *Neuron* **97**, 1253–1260.e1257 (2018).
11. Burrows, E. L. et al. A neuroligin-3 mutation implicated in autism causes abnormal aggression and increases repetitive behavior in mice. *Mol. Autism* **6**, 62 (2015).
12. Uchigashima, M., Cheung, A. & Futai, K. Neuroligin-3: a circuit-specific synapse organizer that shapes normal function and autism spectrum disorder-associated dysfunction. *Front. Mol. Neurosci.* **14**, 749164 (2021).
13. Zhang, Y. et al. An RNA-sequencing transcriptome and splicing database of glia, neurons, and vascular cells of the cerebral cortex. *J. Neurosci.* **34**, 11929–11947 (2014).
14. Zeisel, A. et al. Molecular architecture of the mouse nervous system. *Cell* **174**, 999–1014.e1022 (2018).
15. Stadelmann, C., Timmler, S., Barrantes-Freer, A. & Simons, M. Myelin in the central nervous system: structure, function, and pathology. *Physiol. Rev.* **99**, 1381–1431 (2019).
16. Young, K. M. et al. Oligodendrocyte dynamics in the healthy adult CNS: evidence for myelin remodeling. *Neuron* **77**, 873–885 (2013).
17. Somogyi, P., Freund, T. F. & Cowey, A. The axo-axonic interneuron in the cerebral cortex of the rat, cat and monkey. *Neuroscience* **7**, 2577–2607 (1982).
18. Micheva, K. D. et al. A large fraction of neocortical myelin ensheathes axons of local inhibitory neurons. *Elife* **5**, e15784 (2016).
19. Dubey, M. et al. Myelination synchronizes cortical oscillations by consolidating parvalbumin-mediated phasic inhibition. *Elife* **11**, e73827 (2022).
20. Borges, B. C., Meng, X., Long, P., Kanold, P. O. & Corfas, G. Loss of oligodendrocyte ErbB receptor signaling leads to hypomyelination, reduced density of parvalbumin-expressing interneurons, and inhibitory function in the auditory cortex. *Glia* **71**, 187–204 (2023).
21. Benamer, N., Vidal, M., Balia, M. & Angulo, M. C. Myelination of parvalbumin interneurons shapes the function of cortical sensory inhibitory circuits. *Nat. Commun.* **11**, 5151 (2020).
22. Fields, R. D. A new mechanism of nervous system plasticity: activity-dependent myelination. *Nat. Rev. Neurosci.* **16**, 756–767 (2015).
23. Monje, M. Myelin plasticity and nervous system function. *Annu. Rev. Neurosci.* **41**, 61–76 (2018).
24. Kaller, M. S., Lazari, A., Blanco-Duque, C., Sampaio-Baptista, C. & Johansen-Berg, H. Myelin plasticity and behaviour-connecting the dots. *Curr. Opin. Neurobiol.* **47**, 86–92 (2017).
25. Pan, S., Mayoral, S. R., Choi, H. S., Chan, J. R. & Kheirbek, M. A. Preservation of a remote fear memory requires new myelin formation. *Nat. Neurosci.* **23**, 487–499 (2020).
26. Pease-Raissi, S. E. & Chan, J. R. Building a (w)rapport between neurons and oligodendroglia: reciprocal interactions underlying adaptive myelination. *Neuron* **109**, 1258–1273 (2021).
27. Steadman, P. E. et al. Disruption of oligodendrogenesis impairs memory consolidation in adult mice. *Neuron* **105**, 150–164.e156 (2020).

28. McKenzie, I. A. et al. Motor skill learning requires active central myelination. *Science* **346**, 318–322 (2014).
29. Xiao, L. et al. Rapid production of new oligodendrocytes is required in the earliest stages of motor-skill learning. *Nat. Neurosci.* **19**, 1210–1217 (2016).
30. Chen, J. F. et al. Enhancing myelin renewal reverses cognitive dysfunction in a murine model of Alzheimer's disease. *Neuron* **109**, 2292–2307.e2295 (2021).
31. Wang, F. et al. Enhancing oligodendrocyte myelination rescues synaptic loss and improves functional recovery after chronic hypoxia. *Neuron* **99**, 689–701.e685 (2018).
32. Phan, B. N. et al. A myelin-related transcriptomic profile is shared by Pitt-Hopkins syndrome models and human autism spectrum disorder. *Nat. Neurosci.* **23**, 375–385 (2020).
33. Tabuchi, K. et al. A neuroligin-3 mutation implicated in autism increases inhibitory synaptic transmission in mice. *Science* **318**, 71–76 (2007).
34. Huang, H., He, W., Tang, T. & Qiu, M. Immunological markers for central nervous system glia. *Neurosci. Bull.* **39**, 379–392 (2023).
35. Fang, L. P. et al. Impaired bidirectional communication between interneurons and oligodendrocyte precursor cells affects social cognitive behavior. *Nat. Commun.* **13**, 1394 (2022).
36. Lee, B. Y. & Hur, E. M. A role of microtubules in oligodendrocyte differentiation. *Int. J. Mol. Sci.* **21**, 1062 (2020).
37. Suo, N., Guo, Y. E., He, B., Gu, H. & Xie, X. Inhibition of MAPK/ERK pathway promotes oligodendrocytes generation and recovery of demyelinating diseases. *Glia* **67**, 1320–1332 (2019).
38. Zou, Y. et al. Effect of cytoskeletal linker protein GAS2L1 on oligodendrocyte and myelin development. *Glia* **73**, 840–856 (2025).
39. Hughes, E. G., Kang, S. H., Fukaya, M. & Bergles, D. E. Oligodendrocyte progenitors balance growth with self-repulsion to achieve homeostasis in the adult brain. *Nat. Neurosci.* **16**, 668–676 (2013).
40. Peron, S. P., Freeman, J., Iyer, V., Guo, C. & Svoboda, K. A cellular resolution map of barrel cortex activity during tactile behavior. *Neuron* **86**, 783–799 (2015).
41. Nieto, M. et al. Expression of Cux-1 and Cux-2 in the subventricular zone and upper layers II-IV of the cerebral cortex. *J. Comp. Neurol.* **479**, 168–180 (2004).
42. Canolty, R. T. & Knight, R. T. The functional role of cross-frequency coupling. *Trends Cogn. Sci.* **14**, 506–515 (2010).
43. Hyafil, A., Giraud, A.-L., Fontolan, L. & Gutkin, B. Neural cross-frequency coupling: connecting architectures, mechanisms, and functions. *Trends Neurosci.* **38**, 725–740 (2015).
44. Dvorak, D. & Fenton, A. A. Toward a proper estimation of phase–amplitude coupling in neural oscillations. *J. Neurosci. Methods* **225**, 42–56 (2014).
45. Watrous, A. J., Deuker, L., Fell, J. & Axmacher, N. Phase-amplitude coupling supports phase coding in human ECoG. *eLife* **4**, e07886 (2015).
46. Korotkova, T., Fuchs, E. C., Ponomarenko, A., von Engelhardt, J. & Monyer, H. NMDA receptor ablation on parvalbumin-positive interneurons impairs hippocampal synchrony, spatial representations, and working memory. *Neuron* **68**, 557–569 (2010).
47. Gloveli, T. et al. Orthogonal arrangement of rhythm-generating microcircuits in the hippocampus. *Proc. Natl. Acad. Sci. USA* **102**, 13295–13300 (2005).
48. Stedehouder, J. et al. Fast-spiking parvalbumin interneurons are frequently myelinated in the cerebral cortex of mice and humans. *Cereb. Cortex* **27**, 5001–5013 (2017).
49. Zonouzi, M. et al. Individual oligodendrocytes show bias for inhibitory axons in the neocortex. *Cell Rep.* **27**, 2799–2808.e2793 (2019).
50. Petersen, C. C. H. Sensorimotor processing in the rodent barrel cortex. *Nat. Rev. Neurosci.* **20**, 533–546 (2019).
51. Grubb, M. S. & Burrone, J. Activity-dependent relocation of the axon initial segment fine-tunes neuronal excitability. *Nature* **465**, 1070–1074 (2010).
52. Hu, H. & Jonas, P. A supercritical density of Na^+ channels ensures fast signaling in GABAergic interneuron axons. *Nat. Neurosci.* **17**, 686–693 (2014).
53. Hamada, M. S. & Kole, M. H. Myelin loss and axonal ion channel adaptations associated with gray matter neuronal hyperexcitability. *J. Neurosci.* **35**, 7272–7286 (2015).
54. Berret, E., Kim, S. E., Lee, S. Y., Kushmerick, C. & Kim, J. H. Functional and structural properties of ion channels at the nerve terminal depends on compact myelin. *J. Physiol.* **594**, 5593–5609 (2016).
55. Mei, F. et al. Micropillar arrays as a high-throughput screening platform for therapeutics in multiple sclerosis. *Nat. Med.* **20**, 954–960 (2014).
56. Liu, J. et al. Clemastine enhances myelination in the prefrontal cortex and rescues behavioral changes in socially isolated mice. *J. Neurosci.* **36**, 957–962 (2016).
57. Koenning, M. et al. Myelin gene regulatory factor is required for maintenance of myelin and mature oligodendrocyte identity in the adult CNS. *J. Neurosci.* **32**, 12528–12542 (2012).
58. Ameis, S. H. & Catani, M. Altered white matter connectivity as a neural substrate for social impairment in autism spectrum disorder. *Cortex* **62**, 158–181 (2015).
59. Khanbabaei, M. et al. Precocious myelination in a mouse model of autism. *Transl. Psychiatry* **9**, 251 (2019).
60. Kasuga, Y., Fudge, A. D., Zhang, Y. & Li, H. Characterization of a long noncoding RNA Pcdh17it as a novel marker for immature premyelinating oligodendrocytes. *Glia* **67**, 2166–2177 (2019).
61. Klune, C. B., Jin, B. & DeNardo, L. A. Linking mPFC circuit maturation to the developmental regulation of emotional memory and cognitive flexibility. *Elife* **10**, e64567 (2021).
62. Erzurumlu, R. S. & Gaspar, P. Development and critical period plasticity of the barrel cortex. *Eur. J. Neurosci.* **35**, 1540–1553 (2012).
63. Marques, S. et al. Oligodendrocyte heterogeneity in the mouse juvenile and adult central nervous system. *Science* **352**, 1326–1329 (2016).
64. Nelson, S. B. & Valakh, V. Excitatory/inhibitory balance and circuit homeostasis in autism spectrum disorders. *Neuron* **87**, 684–698 (2015).
65. Cardin, J. A. et al. Driving fast-spiking cells induces gamma rhythm and controls sensory responses. *Nature* **459**, 663–667 (2009).
66. Orefice, L. L. et al. Peripheral mechanosensory neuron dysfunction underlies tactile and behavioral deficits in mouse models of ASDs. *Cell* **166**, 299–313 (2016).
67. Chen, Q. et al. Dysfunction of cortical GABAergic neurons leads to sensory hyper-reactivity in a Shank3 mouse model of ASD. *Nat. Neurosci.* **23**, 520–532 (2020).
68. Michaelson, S. D. et al. SYNGAP1 heterozygosity disrupts sensory processing by reducing touch-related activity within somatosensory cortex circuits. *Nat. Neurosci.* **21**, 1–13 (2018).
69. Polepalli, J. S. et al. Modulation of excitation on parvalbumin interneurons by neuroligin-3 regulates the hippocampal network. *Nat. Neurosci.* **20**, 219–229 (2017).
70. Zhang, B. et al. Developmental plasticity shapes synaptic phenotypes of autism-associated neuroligin-3 mutations in the calyx of Held. *Mol. Psychiatry* **22**, 1483–1491 (2017).
71. Proctor, D. T. et al. Axo-glial communication through neurexin-neuroligin signaling regulates myelination and oligodendrocyte differentiation. *Glia* **63**, 2023–2039 (2015).
72. Bai, X., Kirchhoff, F. & Scheller, A. Oligodendroglial GABAergic signaling: more than inhibition! *Neurosci. Bull.* **37**, 1039–1050 (2021).
73. Habermacher, C., Angulo, M. C. & Benamer, N. Glutamate versus GABA in neuron-oligodendroglia communication. *Glia* **67**, 2092–2106 (2019).

74. Kougioumtzidou, E. et al. Signalling through AMPA receptors on oligodendrocyte precursors promotes myelination by enhancing oligodendrocyte survival. *Elife* **6**, e28080 (2017).
75. Li, J., Miramontes, T. G., Czopka, T. & Monk, K. R. Synaptic input and Ca^{2+} activity in zebrafish oligodendrocyte precursor cells contribute to myelin sheath formation. *Nat. Neurosci.* **27**, 219–231 (2024).
76. Chattopadhyaya, B. et al. Experience and activity-dependent maturation of perisomatic GABAergic innervation in primary visual cortex during a postnatal critical period. *J. Neurosci.***24**, 9598–9611 (2004).
77. Rivers, L. E. et al. PDGFRA/NG2 glia generate myelinating oligodendrocytes and piriform projection neurons in adult mice. *Nat. Neurosci.* **11**, 1392–1401 (2008).
78. Emery, B. et al. Myelin gene regulatory factor is a critical transcriptional regulator required for CNS myelination. *Cell* **138**, 172–185 (2009).
79. Jamain, S. et al. Mutations of the X-linked genes encoding neuroligins NLGN3 and NLGN4 are associated with autism. *Nat. Genet.* **34**, 27–29 (2003).
80. Ma, X. R. et al. Restoring nuclear entry of Sirtuin 2 in oligodendrocyte progenitor cells promotes remyelination during ageing. *Nat. Commun.* **13**, 1225 (2022).
81. Chen, Y. et al. Isolation and culture of rat and mouse oligodendrocyte precursor cells. *Nat. Protoc.* **2**, 1044–1051 (2007).
82. Niu, J. et al. An efficient and economical culture approach for the enrichment of purified oligodendrocyte progenitor cells. *J. Neurosci. Methods* **209**, 241–249 (2012).
83. Xiao, L. et al. Diosgenin promotes oligodendrocyte progenitor cell differentiation through estrogen receptor-mediated ERK1/2 activation to accelerate remyelination. *Glia* **60**, 1037–1052 (2012).
84. Luo, W. et al. Remyelination in neuromyelitis optica spectrum disorder is promoted by edaravone through mTORC1 signaling activation. *Glia* **71**, 284–304 (2023).

Acknowledgements

This work was supported by STI 2030-Major Project of China (2021ZD0201703 to L.X.); National Natural Science Foundation of China (32170957 and 31970913 to L.X.; U22A20306 to J.-h.L. (Jianhong Luo)); Guangdong Basic and Applied Basic Research Foundation (2021A1515012156 to L.X.); and the Key-Area Research and Development Program of Guangdong Province (2019B030335001 to L.X.), and Striving for the First-Class, Improving Weak Links and Highlighting Features (SIH) Key Discipline for Psychology in South China Normal University. The authors would like to express their appreciation to Prof. William David Richardson (UCL) for his critical reading and kind help in editing the manuscript.

Author contributions

L.X. acquired funding, supervised the research, provided research resources. L.X., Y.-x.H., H.-l.L. and J.-h.L. (Jianhong Luo) conceptualize and develop the methodology. Y.-x.H. performed the in vivo recordings. J.L. performed the acute slice electrophysiology. Y.-x.H., W.Z. and J.-h.L. (Junhong Liu) performed the behavioral experiments and immunohistochemical experiments. Y.-x.H., W.Z. and J.-h.L. (Junhong Liu) analyzed the data with help from S.-t.T., T.-y.G., Y.-q.Y., Z.p.-.M., Y.-h.H. and S.-m.W. J.-w.Z. and Z.-j.D. performed transmission electron microscopy. Y.-p.Z., C.-y.T. and L.Y. performed the cell culture experiments. Y.-x.H. and L.X. wrote the manuscript. G.-q.G. provided the in vitro electrophysiology experiment platform. All other authors contributed to the review and editing.

Competing interests

The authors declare no competing interests.

Additional information

Supplementary information The online version contains supplementary material available at https://doi.org/10.1038/s41467-025-61455-0.

Correspondence and requests for materials should be addressed to Lin Xiao.

Peer review information *Nature Communications* thanks Ning Cheng, Domna Karagogeos and the other anonymous reviewer(s) for their contribution to the peer review of this work. A peer review file is available.

Reprints and permissions information is available at http://www.nature.com/reprints

Publisher's Note Springer Nature remains neutral with regard to jurisdictional claims in published maps and institutional affiliations.

[1]Key Laboratory of Brain, Cognition and Education Sciences of Ministry of Education, Institute for Brain Research and Rehabilitation, Guangdong Key Laboratory of Mental Health and Cognitive Science, and Center for Studies of Psychological Application, South China Normal University, Guangzhou, China. [2]Neuroscience Laboratory for Cognitive and Developmental Disorders, Department of Anatomy, Medical College of Jinan University, Guangzhou, China. [3]Department of Pathology of Sir Run Run Shaw Hospital and Department of Human Anatomy, Histology and Embryology, System Medicine Research Center, Center for Neuroscience, NHC and CAMS Key Laboratory of Medical Neurobiology, Center of Cryo-Electron Microscopy, Zhejiang University School of Medicine, Hangzhou, China. [4]Department of Neurology, The Third Affiliated Hospital of Sun Yat-Sen University, Guangzhou, China. [5]Affiliated Mental Health Center & Hangzhou Seventh People's Hospital, School of Brain Science and Brain Medicine, Zhejiang University School of Medicine, Hangzhou, China. [6]Wolfson Institute for Biomedical Research, University College London, London, UK. [7]These authors contributed equally: Yongxiang He, Jiong Li, Wei Zheng, Junhong Liu. ✉e-mail: liuyangxiaolin@aliyun.com